IMOS 2022
Aveiro · Portugal

Iberic Meeting of Optics Students 2022

Book of Abstracts

13 to 15 June 2022

Universidade de Aveiro
Aveiro, Portugal

universidade de aveiro
theoria poiesis praxis

Ficha Técnica

Organização

Apoios

Contents

1   Organization

Local Organizing Committee

Beatriz Oliveira . . . . IT, Universidade de Aveiro

Bruno Brandão . . . . IT, Universidade de Aveiro

Liliana Sousa . . . . IT, Universidade de Aveiro

Marco Fernandes . . . . IT, Universidade de Aveiro

Sara Mantey . . . . IT, Universidade de Aveiro

Rogério Nogueira . . . . IT, Universidade de Aveiro

Iberic Organizing Committee

Amal Zaytouny . . . . IOPTICA, Spanish National Research Council

Carmen Martín . . . . Physics League, University of Valencia

Elena Pascual . . . . Physics League, University of Valencia

Iván Reyes . . . . Physics League, University of Valencia

Néstor Tejedor . . . . IOPTICA, Spanish National Research Council

Pablo Santafé . . . . IOPTICA, Spanish National Research Council

Rocío Gutiérrez Contreras . . . . IOPTICA, Spanish National Research Council

Sara El Aissati Aissati . . . . IOPTICA, Spanish National Research Council

Honorary Committes

Ana Álvarez . . . . Physics League, University of Valencia

Carmen Lago . . . . IOPTICA, Spanish National Research Council

Cátia Pinho . . . . IT, Universidade de Aveiro

Iñigo Chacartegui . . . . Physics League, University of Valencia

Jorge Cuellar . . . . Physics League, University of Valencia

Mariana Ramos . . . . IT, Universidade de Aveiro

Vanessa Duarte . . . . IT, Universidade de Aveiro

Victor Rodriguez . . . . IOPTICA, Spanish National Research Council

Scientific Committee

Ana Rocha . . . . Instituto de Telecomunicações

Carlos D. S. Brites . . . . CICECO, Universidade de Aveiro

Fátima Domingues ....Instituto de Telecomunicações

Fernando Guiomar ....Instituto de Telecomunicações

Gil Fernandes ....Instituto de Telecomunicações

Margarida Facão ....i3N, Universidade de Aveiro

Maria do Carmo Medeiros ....IT, Universidade de Coimbra

Miguel Drummond ....Instituto de Telecomunicações

Nélia Alberto ....Instituto de Telecomunicações

Nelson Muga ....Instituto de Telecomunicações

Nuno Silva ....Instituto de Telecomunicações

Paulo Monteiro ....IT, Universidade de Aveiro

Ricardo Oliveira ....Instituto de Telecomunicações

2 Plenary Speeches

2.1 Topological optical forces

Speaker: Professor Humberto Michinel

Speaker Biography:

Prof. Humberto Michinel is Full Professor of the Applied Physics Dept. of the University of Vigo at Ourense (Spain) and group leader of the Engineering Physics Lab since 1999. His current research is in nonlinear and quantum systems, lasers and photonics. Dr. Michinel is also secretary of the International Commission for Optics (ICO) and was the Past-President of the European Optical Society (EOS) until 2020. He is the CEO and founder of the "spin-off" company "Illumnia" specialized in photonics technologies, co-owned by the University of Vigo. He was the coordinator of the MsC course in "Photonics and Laser Technologies" of the Universities of Vigo, Santiago de Compostela, A Coruña, for the period 2007-2017. He is also the director of the School of Aerospace Engineering at Ourense since 2020.

2.2 Silicon nitride photonics ecosystem: technologies, challenges and opportunities

Speaker: Professor Pascual Munõz

Abstract: The talk will present the evolution of the photonic integrated circuit (PIC) silicon nitride ecosystem in the last decade, describing the key actors in the supply change and the main available open-access technologies. Special emphasis will be made on the importance of using existing micro-fabrication capabilities to create core technologies. This will be put in relation to the current trends in photonic integration, and the challenges and opportunities ahead will be outlined.

Speaker Biography:

Pascual Muñoz (Professor) received his MSc and PhD thesis on Electronic Engineering and Photonics by the Universitat Politecnica de Valencia (UPV), Spain. He is a current Full Professor at the Photonic Research Labs. Prof Muñoz runs a consolidated research line, started in 2005, on prototyping Photonic Integrated Circuits (PICs) in a technology agnostic fashion, where PICs are designed in the best suited technology (Silicon-On-Insulator, Indium Phosphide, Silica on Silicon, Silicon Nitride amongst other) for each application. He has published 50 papers in international refereed journals and over 70 conference contributions. He is a member of the Technical Programme Committees of the European Conference on Optical Communications (ECOC) and the European Conference on Integrated Optics (ECIO). From his research line, he co-founded the UPV spin-off company VLC Photonics in 2011, where the PIC design know-how, expertise and tools have been transferred, and he served as CEO from 2011 to 2013. Since 2011, he is a member of the Board of Directors, where the company strategy is set for the management, and a member of the Joint VLC-UPV R&D Commission, where topics for mutual collaborative and/or contractual research are defined and supervised. Dr. Muñoz is a Senior Member of IEEE and Senior Member of the OSA. His current research encompasses PIC design, silicon nitride technologies and advanced full field PIC test engines. Since 2017, he is leading the initiative to establish UPVfab www.fab.upv.es, the micro-fabrication R&D and pilot line cleanroom facility at UPV.

2.3   Optica Professional Development Talk

Speaker: Yann Amouroux

Speaker Biography:

Yann Amouroux has been at Optica (Formerly OSA) since July 2018, for the last 20+ years he has worked for other Societies such Institute of Engineering and Technology (IET), and before that for many years at the Institute of Physics (IOP).

He is based in Bristol (UK), his responsibilities are to represent Optica to the Optics & Photonics community in Europe, meeting with students, academics, government agencies and industry professionals around numerous countries.

2.4 Photonic Integrated Biosensor Circuits for Ultrasensitive Diagnostics

Speaker: Professor Laura M. Lechuga

Abstract: Biosensor technology based on Silicon Photonics is one of the best prepared to tackle the challenging goal of offering reliable point-of-care diagnostics. To this aim, we develop Nanophotonic biosensors platforms able to provide sensitive, reliable, and selective analysis, while reducing the turnaround times, decreasing and/or eliminating sample transport, and using low sample volume.

Speaker Biography:

Prof. Laura M. Lechuga is Full Professor at the Spanish National Research Council (CSIC) and Head of the Nanobiosensors and Bioanalytical Applications Group at the Catalan Institute of Nanoscience and Nanotechnology (ICN2) in Barcelona (Spain). Her Group is considered as a world reference in this field. The principal focus of her research is the development of novel nanobiosensor devices based on nanoplasmonics and silicon-based photonics principles for point-of-care diagnostics. She has also co-founded two spin-off companies. In addition, from April 2020 to September 2021, she belonged to the Expert Scientific Panel advising the Ministry of Science and Innovation and the Spanish Government in the management of the COVID-19 pandemic.

2.5 Developing Next-Generation Wireless: Terabit Communications Enabled by Free-Space Optics

Speaker: Fernando Guiomar

Speaker Biography:

Dr. Fernando Guiomar is a senior researcher at Instituto de Telecomunicações – Aveiro, where his main research interests are focused within the area of fiber-based and free-space optical communication systems, including the development of digital signal processing algorithms, advanced modulation and coding, constellation shaping and nonlinear modelling and mitigation. In 2015, he has received a Marie Skłodowska-Curie individual fellowship, jointly hosted by Politecnico di Torino, Italy, and CISCO Optical GmbH, Nuremberg. In 2016, he has received the Photonics21 Student Innovation Award, distinguishing industrial-oriented research with high impact in Europe. In 2020, he was awarded a 3-year Junior Leader Fellowship by the "la Caixa" Foundation.

3 Papers

Limitations of Employing Virtual Carrier in the Self-Coherent Detection

Romil K. Patel, Fernando P. Guiomar, Guilherme A. Dominges, Nelson J. Muga, and Armando N. Pinto

Departamento de Eletrónica, Telecomunicações e Informática, Universidade de Aveiro and Instituto de Telecomunicações, Universidade de Aveiro, Aveiro, Portugal.

romilkumar@ua.pt

Abstract: The finite resolution of the digital to analog converter (DAC) imposes limitations on the virtual carrier based self-coherent detection. Results show that ≥ 5 effective number of bits (ENOB) are required to avoid any extra penalty. © 2022 The Author(s)

1. Introduction

The minimum phase signal based self-coherent (SCOH) transceivers can reconstruct phase information of the signal from its intensity profile. This allows the employment of a single photodetector based direct-detection and the recovery of the missing phase information in the digital domain [1]. The SCOH transceiver requires a carrier tone at the edge of the information signal to alleviate the effects of signal to signal beating noise (SSBN) generated upon direct detection [2]. The carrier tone can be added either in radio frequency (RF), optical, or digital domain. Notice that both RF and optical methods increase hardware requirements and complexity. Therefore, a virtual carrier is a viable alternative to get rid of the extra resource requirement [3]. Nevertheless, the virtual carrier incurs an extra penalty due to the finite resolution of the digital to analog converter (DAC). The power of the virtual carrier is kept sufficiently high (higher than the peak to average power ratio (PAPR)) to satisfy the minimum condition requirement. The high power virtual carrier can change the dynamic range of the signal which consequently reduces the effective number of bits (ENOB) of the given DAC and increases quantization noise.

2. Results

Figure 1 presents the results obtained from the simulation analysis of the effects of employing a virtual carrier in the SCOH transmission. We employ a 30 Gbaud 36QAM probabilistic constellation shaping signal for the performance assessment.
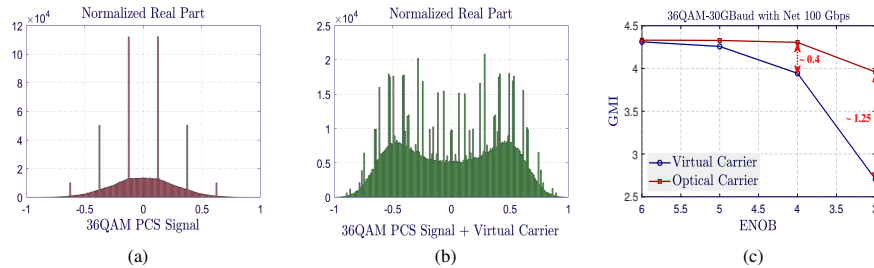

Fig. 1: Obtained simulation results, (a) histogram of 36QAM information signal without virtual carrier (b) histogram of 36QAM information signal + virtual carrier, and (c) impact of virtual carrier on the performance.

Fig. 1a and 1b present the histogram of the pulse shaped 36QAM signal without and with virtual carrier, respectively. The result in 1b shows that the inclusion of a virtual carrier increases the dynamic range of the signal to a great extent. This consequently requires the DAC with sufficiently high ENOB to effectively reduce the quantization noise. Finally, Fig. 1c presents the impact of a virtual carrier in terms of optimum generalized mutual information (GMI) as a function of ENOB of the DAC. The results show that penalties of $\sim$0.4 and $\sim$1.25 GMI loss incurred with the ENOB of 4 and 3, respectively.

3. Conclusions

We performed an extensive analysis of the impact of a virtual carrier in SCOH transmission, which shows that the virtual carrier demands higher than 5 ENOB to significantly alleviate the quantization noise of the DAC.

References

1. A. Shahpari, *et al.*, *Optical Fiber Technology*, Vol. 26, pp. 100-107, Jul., 2015.
2. R. Patel, *et al.*, *Journal of Lightwave Technology*, Vol. 38, pp. 4205-4212, Aug., 2020.
3. R. Patel, *et al.*, *Optics Express*, Vol. 29, pp. 41234-41245, Dec., 2021.

Improved Carrier Contribution Factor Estimation in Self-Coherent Detection

Guilherme A. Domingues, Romil K. Patel, Nelson J. Muga, and Armando N. Pinto

Dep. de Eletrónica, Telecomunicações e Informática, Universidade de Aveiro, e Instituto de Telecomunicações,
3810-193, Aveiro, Portugal

guilhermead@ua.pt

Abstract: We numerically improve the carrier contribution factor (CCF) estimation for the DC-Value self-coherent system. By applying a moving average filter to the original CCF values, the mean relative error was reduced from 1.7% to 0.4%. © 2022 The Author(s)

1. Introduction

Minimum phase signal based self-coherent (SCOH) systems are capable of recovering both phase and amplitude data using a single photodiode when employing the DC-Value (DC-V) method [1]. The DC-V method requires a precise estimation of the carrier contribution factor (CCF), also refered to as E_o parameter, since it is used in the minimum phase condition (MPC) in the phase reconstruction process and a reliable method has been introduced in [2]. This method, however, uses the full data signal to determine the CCF. In a real-time system this is an impractical approach, due to the large amount of data to be processed. In this work, we propose a reliable solution where we decrease the estimation error of the E_o parameter.

2. Carrier Contribution Factor Numerical Analysis

For a precise CCF estimation, two parameters are essencial: the carrier to signal power ratio (CSPR) and the generated photocurrent power. The CCF estimation allows to determine the E_o parameter that is applied to the MPC during the phase reconstruction process. In a simulator developed at Instituto de Telecomunições, named NETXPTO, the data is processed in sequences. This data segmentation originates numerical errors that lead to an innacurate carrier addition and consequently have an impact in estimated E_o. The aforementioned numerical errors are originated from uneven mean values between the data sequences at the transmitter, which impact the received photocurrent power. To minimize the impact of numerical errors in the CCF estimation, we applied a moving average (MA) filter with 32 taps in a 16QAM system with 10 dB of CSPR and the results are presented Fig. 1. The original E_o estimation presents a sinusoidal behaviour and some of its values can reach an error of 5.4%, which surpasses the 5% limit presented in [2]. When applying a MA filter to the values, we get a much more even distribution of the E_o parameter but, most importantly, the values are much closer to its ideal value.
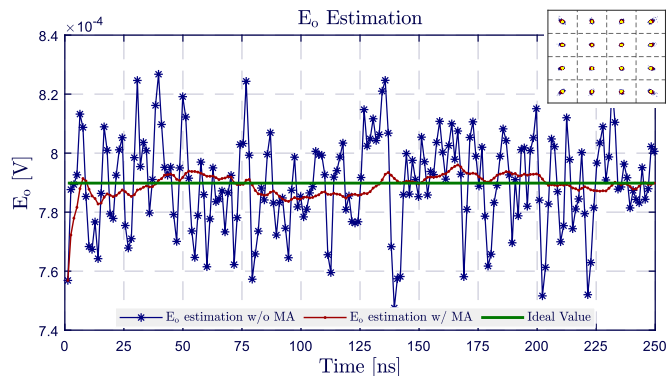
Fig. 1: Comparison of E_o estimations throughout the time using the original and improved CCF, applying a 32 taps MA filter, with ideal E_o. Inset constellation shows symbols w/ MA (red), w/o MA (blue) and reference (yellow).

3. Conclusion

We have successfully improved the CCF estimation by using a MA filter with 32 taps, although a filter with more taps could also be used. This numerical analysis was performed using a 16QAM system with 10 dB of CSPR. The mean error in the E_o parameter estimation decreased from 1.7% to 0.4%. Using this simple technique, we also verified an error vector magnitude (EVM) gain of 2.6 dB.

References
1. R. K. Patel, *et al., Journal of Lightwave Technology*, vol. 38, pp. 4205-4212, Aug., 2020.
2. R. K. Patel, *et al., Optics Express*, vol. 29, pp. 41234-41245, Dec., 2021.

Optimizing Geometric Constellation Shaping
Through End-to-End Deep Learning

Samuel M. Silva, Manuel S. Neves, Beatriz M. Oliveira, Paulo P. Monteiro and Fernando P. Guiomar

Instituto de Telecomunicações, University of Aveiro

samuelms@ua.pt

Abstract: Applying geometric shaping to a constellation is known to improve the performance of the communication system. Here, an Auto-Encoder (AE) was implemented to determine the best geometry of the constellation, and it is demonstrated that it allows reducing the transmitted power by 0.3 dB, when compared to a classical QAM constellation.

1. Introduction

A plethora of services requires a better performance from communication systems. To address that, the order of the constellation is usually increased as a way to raise the bitrate; however, with higher order, comes the need to have an increase in power signal. In order to improve the performance of classical QAM constellations, one can use geometric shaping [1]. This technique determines the best constellation format, depending on the conditions of the communication system, to minimize errors during transmission. One way to do it is by using an AE [2], which is composed of two Neural Networks (NNs): one at the transmitter (encoder) and another at the receiver (decoder). The encoder Neural Network (NN) receives the symbols, and decides which are the best coordinates (in-phase and quadrature) to send them. At the reception, the noisy signal is read by the decoder NN, which determines the most likely area to receive the symbol with minimum error.

2. Methods

To study the AE, a constellation of order 64 was chosen, and it was compared against a square 64-QAM. Both of the systems transmitted 2×10^6 symbols for different Signal to Noise Ratios (SNRs) in the range from 14 up to 21dB. The system with the classical constellation is composed of 3 main blocks: the first is the symbols' generator, another is an Additive White Gaussian Noise (AWGN) channel, and the final one detects which symbol was received. The system with the AE, illustrated in Fig. 1, is composed of 5 main blocks: the first is the symbols' generator; both the second and the fifth are NNs composed of 2 layers: the first one has 64 neurons with a Rectified Linear Unit (ReLU) activation function, and the second layer has 2 neurons (in-phase and quadrature signals), with a linear activation function in the second block and 64 neurons with a Softmax activation function in the fifth block; the third is the normalization of the constellation, before the signal transmission; the fourth block is the AWGN channel. The AE was trained 3 times for each Signal to Noise Ratio (SNR), with five epochs, a batch size of 2×10^4 symbols, and a learning rate of 0.05. For each SNR, the constellation with higher accuracy was selected to assess the AE constellation in the results below.

3. Results

To analyze the results, a graphic with three lines describing the relationship between Symbol Error Rate (SER) and SNR was made (Fig.2). The red line is from the theoretical expression. The blue one is the simulated in our system with a square 64-QAM and the green line are the constellations determined by the AE. The fact that the simulated line overlaps with the theoretical line means that our system was well designed. We can also observe that the constellations from the AE have a gain when compared to the square constellation; as an example, a gain of 0.3dB was measured at a SER of 0.1. The best constellation determined by the AE is presented in the lower left corner of Fig. 2, and it resembles the shape of a Gaussian function.

Fig. 2. SER vs SNR for classical QAM constellations and the AE; the shape of the learned constellation, and respective learned decision regions is visible on the lower left corner.

Fig. 1. Block diagram of the AE system.

4. Conclusions

In this manuscript, an AE based on NNs was implemented to optimize the geometric shaping of the two-dimensional constellation for the AWGN channel. As shown, in the specific case of a 64-ary constellation, the solution converges to a Gaussian-like shape, which results in a gain of 0.3 dB when compared to a classical 64-QAM constellation.

References

[1] J. G. David Forney, R. G. Gallager, G. R. Lang, F. M. Longstaff and S. U. Qureshu, "Efficient Modulation for Band-Limited Channels," September 1984.

[2] T. O'Shea and J. Hoydis, "An Introduction to Deep Learning for the Physical Layer," 2017.

Quantum-Noise Based True Random Number Generation

Maurício J. Ferreira[1], Nuno A. Silva[1], Nelson J. Muga[1]

[1]Instituto de Telecomunicações, University of Aveiro, Campus Universitário de Santiago, 3810-193 Aveiro, Portugal
mauricioferreira@ua.pt

Abstract: A real-time quantum random number generator based on quadrature fluctuations of a vacuum state was implemented and validated, showing support for rates up to 8.23 Gbps. The scheme passes all state-of-the-art randomness evaluation tools. © 2022 The Authors

1. Introduction

Random numbers (RNs) are currently an essential resource in security-critical cryptographic applications. So far, pseudorandom number generators have been able to suppress this demand, but such methods yield inherently periodic sequences that become predictable to an adversary with access to enough computational power [1]. Quantum random number generators (QRNGs) address these questions by exploring the probabilistic nature of quantum measurements as their randomness source [2]. Here, we implement and validate a real-time QRNG based on homodyne measurements of the quadrature fluctuations in a vacuum state of the electromagnetic field.

2. Methods and Results

In the proposed scheme, a strong laser acts as the local oscillator (LO) and interacts with a vacuum state in a balanced beam splitter. Its purity can be guaranteed, at room temperature, by simply blocking one of the input ports [2]. The output signals are posteriorly measured by a balanced detector and the resulting photocurrents are subtracted. Thus, a signal proportional to the amplitude quadrature of the probed state is obtained, which follows a Gaussian distribution [1]. Unfortunately, measurements also contain classical contributions such as electronic noise. Consequently, a randomness extraction (RE) algorithm based on Toeplitz-hashing is applied to suppress them [2].

As seen in Fig.1a, a preponderance of quantum noise was obtained, with an observed quantum-to-classical noise ratio of approximately 11.7 dB, neglecting any LO excess noise. Moreover, we verify that all noise follows the expected null-mean Gaussian distribution. In these conditions, approximately 8.39 random bits per sample can be obtained, supporting generation rates up to 8.23 Gbps. Unfortunately, the length-compatible real-time RE algorithm limits this to an effective throughput of 75 Mbps. Nonetheless, as seen in Fig.1b, the RE is effective in removing any low-order correlations present in the raw sequence, and true RNs are extracted with an upper security bound of 2^{-105}, illustrating the quality of this scheme. Finally, the QRNG was validated and verified to pass all the statistical tests of the NIST, DieHarder, and TestU01's *SmallCrush* batteries, as well as most of TestU01's *Crush* evaluations.
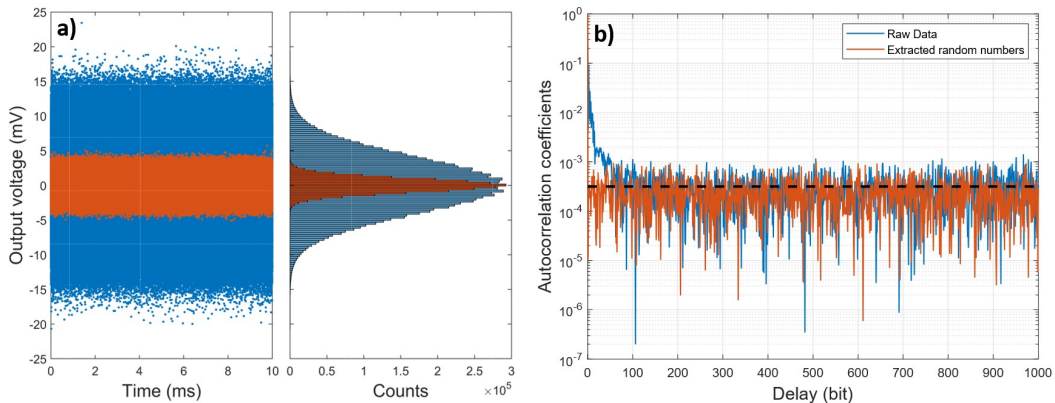
Fig. 1. (a) Distribution of the total (blue) and electronic (orange) noise. (b) Autocorrelation coefficients of the measured noise. Dashed line represents the theoretical standard deviation for the autocorrelation function.

3. References

[1] M. Herrero-Collantes et al., "Quantum random number generators," APS **89**, 015004 (2017)**.**
[2] M. J. Ferreira et al, "Characterization of a Quantum Random Number Generator Based on Vacuum Fluctuations," Appl **11,** 7413 (2021).

CV-QKD Imperfections Impact on Shot-Noise Measurement

Margarida Almeida[1,2,*], Armando N. Pinto[1,2], and Nuno Silva[1]

[1]Instituto de Telecomunicações, University of Aveiro, Campus Universitário de Santiago, 3810-193, Aveiro, Portugal
[2]Department of Electronics, Telecomunications and Informatics, University of Aveiro, 3810-193, Aveiro, Portugal
[*]Corresponding author: mralmeida@ua.pt

Abstract: The impact of experimental imperfections on the shot-noise in homodyne detectors for Continuous-Variable Quantum Key Distribution is analyzed. Poor modeling of the homodyne detectors under-estimates the shot noise creating security loopholes. © 2022 The Author(s)

Quantum key distribution (QKD) is a major application of quantum cryptography [1], with continuous-variable (CV) systems using weak coherent states and homodyne detectors (HDs) for a practical and efficient solution [2]. This makes CV-QKD systems compatible with existing communications systems [2]. An HD monitors the intensity of both outputs of a balanced beam splitter (BS) using two PIN photodetectors (PINs), subtracting, and amplifying the output signal. CV-QKD systems base their security on the receiver's precise estimation of the channel loss and excess noise, requiring HDs with ultra-low noise, high subtraction, and a flat amplification profile [3].

The setup considered is represented in Fig. 1a. This system consists of a local oscillator (LO) laser followed by a Mack-Zehnder amplitude modulator (MZAM), a variable optical amplifier (VOA), and an HD. The HD contains a 50:50 BS followed by two VOAs for rebalancing, two PINs, and a trans-impedance amplifier (TIA). We consider a LO modulation with a 50% duty cycle pulse, an unbalanced BS, and that the PINs have a non-unitary efficiency modulated through a virtual beam splitter (VBS) [3]. Here we study the impact of the TIA response's modeling on the estimation of the output variance. In Fig. 1 we compare the output variance by modeling the TIA as an ideal low pass (LP) filter and as a Butterworth (BW) filter of order 3. Assuming the TIA to be modeled as an ideal LP filter, unfeasible for any practical HD, can lead to security loopholes when HDs are used in CV-QKD systems since the estimated output variance is smaller than its true value. This both considering the unbalanced (Fig. 1b) and the rebalanced (Fig. 1c) configurations of the HD [3]. The BS's unbalance results in a quadratic evolution of the variance with the optical power of the LO (Fig. 1b), due to the LO's relative intensity noise. In the rebalanced configuration, the HD recovers its ideal linear behavior, being limited only by the shot noise. Remark that, in a practical CV-QKD system usually only the thermal noise and the shot noise are estimated. The poor modeling of the TIA response can mislead the estimation of the output variance, being this under-estimation more critical in case the system is not compensated for its unbalances.

To summarize, we discuss the impact of experimental imperfections of HDs on the output voltage variance, namely the unbalance of HD and the modeling of the TIA in the HD, showing that erroneous modeling of the TIA can lead to an under-estimation of the voltage variance and thus open security loopholes in CV-QKD systems.
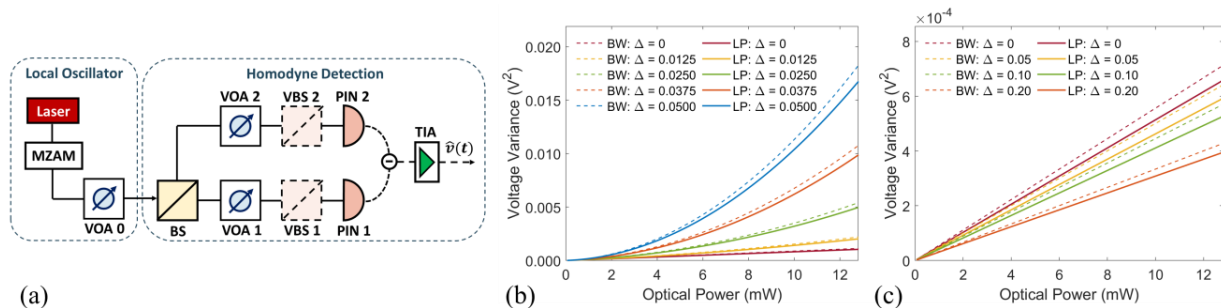
Fig. 1. (a) Schematic setup of a HD. Noise voltage variance for (b) an unbalanced HD, (c) a rebalanced HD.

References
[1] Loura, R. et al. Noise and measurement errors in a practical two-state quantum bit commitment protocol. Phys. Rev. A **89**, 052336 (2014).
[2] Pirandola, S. et al. Advances in Quantum Cryptography. Adv. Opt. Photon. **12**, 1012 (2020).
[3] Almeida, M. et al. Impact of imperfect homodyne detection on measurements of vacuum states shot noise. Opt Quant Electron **52**, 503 (2020).

Production of Water-soluble Fluorescent Carbon Quantum Dots through Nanosecond Pulsed Laser Ablation in Liquid

Francis Rey Cortes*[1], Mitzi Ordoñez-Pérez[1], Eva Falomir[2], Gladys Mínguez-Vega[1]

[1]*Group of Optics-UJI (GROC-UJI), Institute of New Imaging Technologies (INIT), Universitat Jaume I (UJI), 12071, Castellón, Spain*
[2]*Department of Inorganic and Organic Chemistry, Universitat Jaume I (UJI), 12071, Castellón, Spain*
* Email: frcortes@uji.es

Abstract: Water-soluble fluorescent carbon quantum dots (CQDs) are created by implementing nanosecond laser ablation technique. The addition of water in a resulting colloidal solution does not affect the fluorescence emission and surface states of CQDs. © 2022 The Author(s)

1. Introduction

Carbon quantum dots (CQDs) as a novel fluorescent carbon nanomaterial, gained a considerable amount of attention due to their attractive properties such as green synthesis, low cost and abundant precursors, photostability, low toxicity, excellent water solubility and tunable fluorescence emission in comparison to fluorescent semiconductor-based quantum dots and conventional dyes. Based on these excellent properties, CQDs shows a great potential in numerous applications such as biosensing, chemical sensing, drug delivery, bioimaging and photocatalysis. [1]

Generally, CQDs can be synthesized using microwave-based process, ultrasonication, solvothermal treatment, arc discharge, chemical oxidation in strong acid, laser ablation or electrochemical method. Compared to all synthesis routes, laser ablation becomes more dominant because of its simple, straightforward and as well as its greener approach which avoids unnecessary toxic by-products. However, the major setback that this method faced at this time is that most of the liquid environment used are organic solvents which limits the full capacity of CQDs in biomedical and biological applications [2, 3]. Thus, in this work, we used nanosecond (*ns*) pulsed laser ablation to synthesize water-soluble fluorescent CQDs starting from carbon black powders (< 100 nm) dispersed in ethanol. Then the resulting colloidal solution was irradiated by adding water constantly with the same laser parameters as before.

2. Results and Discussion

Fig 1a shows a TEM image of CQDs at 10 nm resolution. It can be observed that our CQDs are quasi-spherical with the average size of 1.5 nm as shown in the inset image. Figure 1b shows the steady-state photoluminescence (PL) emission spectra of our CQDs. The emission profile exhibits the excitation-wavelength dependent PL emission. The inset image shows the fluorescence of CQDs solution under 365 nm lamp. In conclusion, the addition of water in reirradiation does not significantly disrupt the fluorescence of our CQDs.
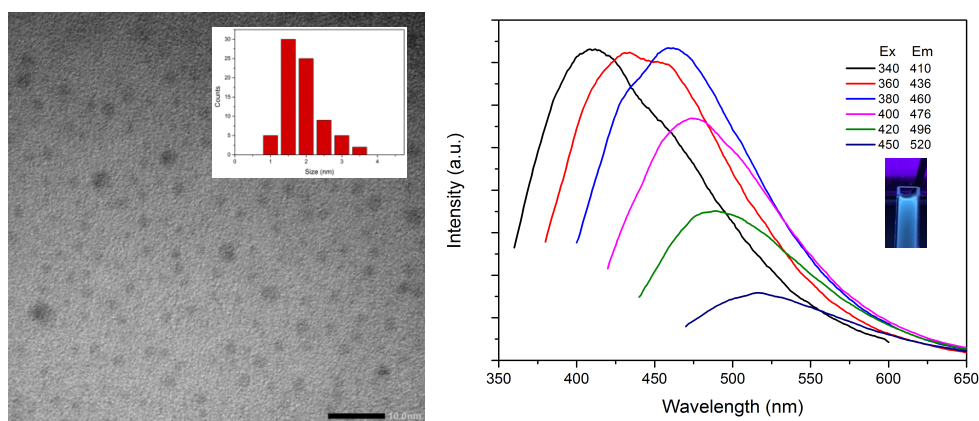
Figure 1 (a) TEM image at 10 nm resolution and (b) PL emission spectra of CQDs.

3. References

[1] A. Singh, et. al. "Self-functionalized ultrastable water suspension of luminescent carbon quantum dots", MCP, vol. 225 (2019).
[2] G.K. Yogesh, et. al. "Synthesis of water-soluble CNPs from ns pulsed laser ablation in ethanol", OLT, vol. 135 (2021).
[3] C. Doñate-Buendia, et. al. "Fabrication by laser irradiation in a continuous flow jet of carbon quantum dots for fluorescence imaging", ACS Omega, 2735-2742 (2018).

Theoretical analysis of Raman based DTS, using a 1064 nm pump source

Joana Vieira[1,2]*, Rogério Nogueira[1], A. M. Rocha[1]
[1]Institute of Telecommunications, Campus de Santiago, 3810-193 Aveiro, Portugal
[2]University of Aveiro, Campus Universitário de Santiago, 3810-193 Aveiro, Portugal
*joana.saraiva.vieira@av.it.pt

Abstract: A theoretical analysis of a Raman backscatter based distributed optical fiber temperature sensor is presented. A pump wavelength of 1064 nm and standard single mode fiber was considered.
© 2022 The Author(s)

Distributed optical fiber sensors (DOFSs) are intrinsic optical fiber sensors, where all the fiber length is used as sensing element, providing continuous measurements distributed along the fiber. The most mature technologies for distributed temperature sensing (DTS) are based on the detection of Raman backscattering using optical-time-domain-reflectometry (OTDR) configurations, in which the temperature is obtained from the ratio between the Raman anti-Stokes (AS) and Stokes (S) powers [1]. The use of installed standard singlemode fiber-based telecommunication networks as sensor systems together with the data transmission can have great interest, as reported in [2]. Here, a possible solution for this type of system is evaluated, a Raman based DTS system is analyzed by theoretical modeling considering a pump source with a wavelength chosen outside of the telecommunications' transmission windows, i.e., 1064 nm. The model developed is based in [3], and estimates the backscattered Raman power for the S and AS bands, according to equations (1) and (2), generated in a short fiber region (Δz), related with the spatial resolution of the DTS system. The S and AS powers also depend on the input pump pulse peak power P_0, the Bose-Einstein probability distribution of phonons ρ, the Raman capture coefficients τ and on the effective power attenuation coefficients α_P, each specific for S and AS band. Δz depends on the vacuum light velocity c, the pump pulse width Δt and on the group refractive index of the core of the fiber n. Here, we considered a pump with pulse width of 10 ns ($\Delta z = 1$ m), for which the S and AS bands are expected to be centered at the wavelength of 1115 nm and 1015 nm, respectively, and different peak pulse powers. Furthermore, the polarization state of the pump is not considered. A fiber with 5000 m at a temperature of 300 K, except for a section with a temperature of 350 K is studied.

Fig. 1 shows a decrease of the Raman backscatter power generated in each section with the fiber length. It is also observed that higher pump pulse peak power results in higher backscattered power of both S and AS bands. As expected, for higher temperature, the backscattered power increases, and this increase is higher for the AS band (42%) than for the S band (5%).

$$P_S(z,0) = P_0 \rho_S \tau_S \Delta z e^{-2\alpha_{P,S}z} \tag{1}$$

$$P_{AS}(z,0) = P_0 \rho_{AS} \tau_{AS} \Delta z e^{-2\alpha_{P,AS}z} \tag{2}$$
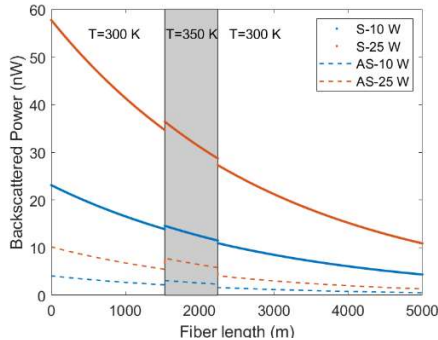
$$\Delta z = \frac{c\Delta t}{2n} \tag{3}$$

Fig. 1. Backscattered Raman power of S and AS bands as function of fiber length for pump pulses peak powers of 10 W and 25 W and equations used.

References
[1] P. Lu *et al.*, "Distributed optical fiber sensing: Review and perspective," *Applied Physics Reviews*, vol. 6, no. 4, 2019, doi: 10.1063/1.5113955.
[2] G. A. Wellbrock *et al.*, "First field trial of sensing vehicle speed, density, and road conditions by using fiber carrying high speed data," *Optics InfoBase Conference Papers*, vol. Part F160-, pp. 2019–2021, 2019, doi: 10.1364/ofc.2019.th4c.7.
[3] M. A. Farahani and T. Gogolla, "Spontaneous Raman scattering in optical fibers with modulated probe light for distributed temperature Raman remote sensing," *Journal of Lightwave Technology*, vol. 17, no. 8, pp. 1379–1391, 1999, doi: 10.1109/50.779159.

Surface Enhanced Raman Scattering mediated by decorated graphene oxide with metal nanoparticles

Sergio Molina-Prados*[1], Ana Cros[2], Gladys Mínguez-Vega[1] & Núria Garro*[2]

[1] *GROC·UJI, Institut de Noves Tecnologíes de la Imatge (INIT), Universitat Jaume I, Spain.*
[2] *Institut de Ciència dels Materials (ICMUV), Universitat de València, Spain.*
e-mail: molinapr@uji.es nuria.garro@uv.es

Abstract: The reproducibility and enhancement factor of Surface Enhanced Raman Scattering improve when using hybrid substrates of metal nanoparticles and graphene oxide. The role of NPs-GO coupling is addressed by means of co-localization AFM-Raman scattering maps. © 2022 The Author(s)

1. Introduction

Raman spectroscopy provides a fingerprint of the composition and structure of most materials in a fast and non-destructive way. However, the efficiency of Raman scattering is much lower than other optical processes. One way to increase Raman intensity is through Surface Enhanced Raman Scattering (SERS), a spectroscopic technique that has improved the efficiency up to 10 orders of magnitude. This phenomenon is explained by the coupling of light with plasmons in metallic nanostructures [1]. The most important drawback of SERS is the inconsistency in intensities and the occurrence of spurious peaks. However, a promising solution is the use of two-dimensional materials. We propose using hybrid substrate based on graphene oxide (GO) sheets decorated with colloidal metal nanoparticles (NPs) synthesized by the laser ablation technique [2]. This structure is known as G-SERS substrate.

For the sample preparation, we synthesized the NPs colloid by pulsed laser ablation in liquids (PLAL) using a Nd:YAG nanosecond laser. For G-SERS substrates when metal NP colloid and GO solution are mixed, they are attached by electrostatic effect. Then, using the drop-casting technique, the NPs and GO-NPs solutions are deposited on flat substrate for further characterization. Methylene blue (MB) is deposited as a probe molecule on SERS and G-SERS substrates and displays a clear increase in the Raman intensity, as shown in Fig. 1a). To understand the role of the GO in SERS stabilization, G-SERS substrates have been characterized by Atomic Force Microscopy (AFM) to perform Kelvin Probe Force Microscopy (KPFM) measurements [3]. In this way, maps of topography and surface potential of the substrate can be correlated with maps of the enhancement factor (EF) of G-SERS, see Fig. 1b)-d).

In this work, efficient G-SERS substrates for Raman spectroscopy and molecule detection have been prepared. It is observed that the high intensity region is found on the NPs decorated GO films while it is not possible to detect MB Raman scattering in absence of NPs. Raman intensity and reproducibility have been shown to increase using G-SERS substrates. Due to the AFM-Raman co-localized study, we can correlate the relative position and electrical coupling of the NPs with the increase in Raman scattering efficiency. In this way, we can characterize the substrates by obtaining the areas with the greatest increase in SERS.

2. Figures
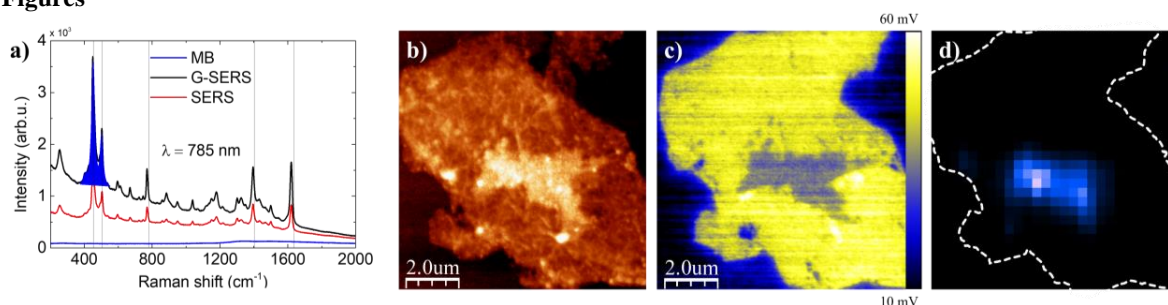
Fig. 1. a) MB spectra using conventional Raman scattering, SERS, and G-SERS substrates with Au NPS. b) Image of the surface topography of a GO film decorated with Au NPs, scaled from 0 to 60 nm. c) Image of the surface potential, scaled from 10 to 60 mV. d) High SERS intensity areas due to the existence of hot spots in the film.

3. References

[1] M. Ali Tahir and Nicoleta E. Dina; *Nanoscale*, **13**, 11593 (2021).
[2] R. Torres-Mendieta and D. Ventura-Espinosa; *Scientific Reports*, **6**, 30478 (2016).
[3] L. Z. Cheong and W. Zhao; *Acta Biomaterialia*, **99**, 33–52 (2019).

Impact of noise in stereoscopic vision aided by structured light

Victor GONCALVES (1,2) , Paulo P.Monteiro (2), Miguel V. Drummond(2)

(1) ENSICAEN, 14000 Caen, France

(2) Instituto de Telecomunicações, University of Aveiro, Campus Universitário de Santiago, 3810-193, Aveiro Portugal

victor.goncalves@ecole.ensicaen.fr

Abstract: Although the proposed stereoscopic LiDAR has a simple concept, turning it into a prototype involves many important details, starting by coding a realistic simulation model, generating the spot, minimizing noise, and configuring cameras for receiving the signal. © 2022 The Author(s)

1. Introduction

Self-driving cars have been "just around the corner" for some years already. The main reason is safety: safe self-driving cars require vision sensors, namely cameras, RADARs and LiDARs. Even though such vision sensors have complementary advantages and drawbacks (see here), LiDAR is the sensor capable of providing a detailed 3D view of the surroundings: the point cloud. However LiDARs is by far the most expensive vision sensors.

The approach to make an inexpensive LiDAR is to resort to stereo vision, as depicted in the scheme Fig.1. The scheme relies on a pair of inexpensive cameras (the eyes), which capture a dot pattern projected by a simple laser. Estimating the distance to an obstacle illuminated by a laser dot can be done by resorting to trivial triangulation. However we need to quantify the impact of noise in the final estimation.

2. Methods

We need firstly to generate the spot and after to pixelate the spot (View of the camera). After we need to simulate the impact of the noise (electronics noise, dark noise, shot noise). Thank these simulations, we will choose if we need a filter before the camera and/or we need a better camera. We will then confirm the simulation results by experimental validation.
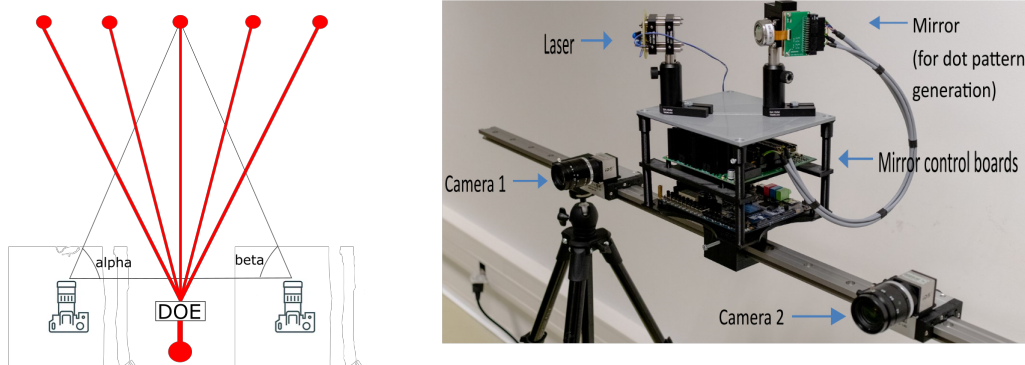

Fig. 1. Left: proposed stereoscopic LiDAR. Right: implemented system.

References

Renato Afonsoc, "Spacial domain LiDAR", MSc thesis, Universidade de Aveiro, 2019

3D object detection for self driving vehicles aided by object velocity

Leandro Alexandrino[1,2]**, Pétia Georgieva**[1]**, Hadi Z. Olyaei**[2]**, André Albuquerque**[2]
and Miguel V. Drummond[1]

[1] *Instituto de Telecomunicações, Departamento de Electrónica, Telecomunicações e Informática, Universidade de Aveiro, 3810-193 Aveiro, Portugal*

[2] *Bosch Car Multimedia, Braga, Portugal*

Abstract: In this paper the preliminary results of the impact of object velocity on 3D object detection are presented using a synthetic dataset and PointPillars model.   © 2022 The Author(s)

1.   Introduction

Coherent LIDARs allow the simultaneous measurement of velocity and range, however, to our knowledge, there is no study regarding the impact of velocity on 3D object detection. Furthermore, there are no datasets with such information available online, therefore, to study a potential improvement introduced by velocity, one must generate a synthetic dataset. Using Grand Theft Auto V (GTA V) commercial videogame and taking advantage of the large modding community, one can use GTA V native functions to obtain object information, such as the velocity, without inference. To create a point cloud, PreSIL [1] will be used as this source code has a virtual LIDAR implemented and the generated dataset follows KITTI's [2], enabling consistent datasets. Regarding the Deep Learning model, PointPillars was chosen due to it's simplicity and due to being a model that enables good performance on low training times while also being available on OpenPCDet [3] which is a framework that eases the process of training, evaluating and optimizing the models.
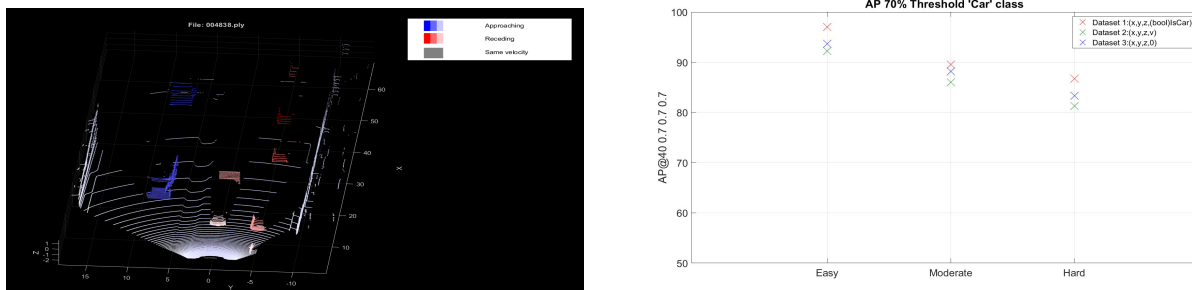
Fig. 1. On the left: Example of a point cloud with relative velocity per-point acquired through GTA V. On the right: PointPillars Average Precision on 'Car' class with 70% threshold.

2.   Preliminary results

The results obtained thus far are presented in Figure 1 using 3 datasets. Dataset 1 is a dataset where points that belong to the 'Car' object class will have 1.0 velocity, other points have 0.0 velocity. In the Dataset 2 every point of the point cloud will have a relative velocity value. At last, Dataset 3 is a zero-velocity dataset in which every point of the point cloud has 0.0 velocity.

References

1. B. Hurl, K. Czarnecki, S. L. Waslander, "Precise Synthetic Image and LiDAR (PreSIL) Dataset for Autonomous Vehicle Perception", https://arxiv.org/abs/1905.00160.
2. A. Geiger, P. Lenz, C. Stiller, R, Urtasun, "Vision meets Robotics: The KITTI Dataset", http://www.cvlibs.net/publications/Geiger2013IJRR.pdf.
3. OpenPCDet Development Team, "OpenPCDet", https://github.com/open-mmlab/OpenPCDet.

New automotive LiDAR estimation techniques

Daniel Bastos[*], **Abel Lorences-Riesgo**[+], **Paulo Monteiro**[*], **Arnaldo Oliveira**[*],
Dionísio Pereira[†], **Hadi Olyaei**[†], **Miguel Drummond**[*]

[*]*Instituto de Telecomunicações and Universidade de Aveiro, Aveiro, Portugal*
[+]*Huawei Technologies France, Paris, France;* [†]*Bosch Car Multimedia Braga, Braga, Portugal*
d.bastos@ua.pt

Abstract: Novel automotive LiDAR methods for application to full-waveform LiDAR data were developed. Such methods show great estimation performance, while being simpler to implement than other mainstream LiDAR techniques. © 2022 The Author(s)

1. Introduction

The latest news regarding autonomous driving reveal that level 5 autonomy is a reality still very distant into the future. In order to achieve such a feat, several technological breakthroughs need to occur both in terms of the perception and the autonomous control parts of a vehicle. Regarding the perception, light detection and ranging (LiDAR) sensors are very important, due to the high spatial and angular resolution depth measurements they can make from short to long ranges (300 m). Such information may be combined with camera frames, to easily generate 3D images of the vehicles surroundings or with other sensor data, to achieve redundant and fail-proof perception [1]. The work herein presented shows a novel LiDAR estimation technique, that can mitigate some of the drawbacks observed in current automotive LiDARs, while requiring a simple receiver architecture.

2. Methods and results

The novelty of the developed method is the combined analysis of the samples of the captured signal in both time and frequency domains, obtaining a coarse and a fine delay estimation, respectively from each domain. Both estimations are then combined and properly calibrated to get a precise and accurate final LiDAR estimation. Several ways to combine such measurements were tested and evaluated. The developed LiDAR estimation techniques were tested using signals acquired with the experimental setup of Fig. 1a), where: a short pulse was generated with a 1550 nm MOPA laser, transmitted through a channel emulator whose total attenuation was digitally controlled with a VOA, and received with an APD, Thorlabs APD430C/M, whose output signal was sampled with a real-time scope (RTS), Keysight DSOS904A. A dynamic range of 45 dB was emulated with such setup and several captures were performed for each tested attenuation. Some of the averaged captured signals are shown in Fig. 1b). The received waveforms were also digitally delayed to evaluate the performance of the methods. The performance of one of the developed methods is shown in Fig. 1c), where a sub-cm precision and accuracy is achieved over a wide dynamic range, even when the optical receiver is saturated and the pulses are severely distorted.

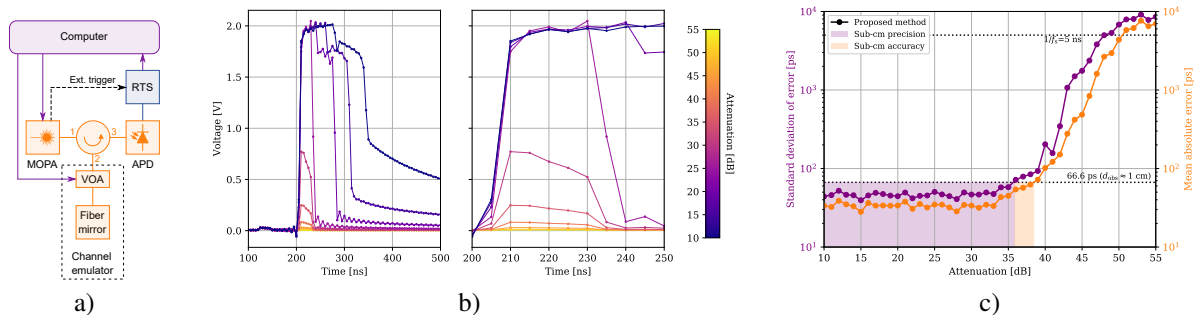Fig. 1. a) Experimental setup. b) Received signals averaged across all captures. c) Standard deviation (STD) of estimation error and mean absolute error (MAE), evaluated over all delays and captures.

References

1. Y. Li and J. Ibanez-Guzman, "Lidar for Autonomous Driving: The Principles, Challenges, and Trends for Automotive Lidar and Perception Systems," IEEE Signal Process. Mag. **37**, 50–61 (2020).

Experimental Demonstration of a Visible Light Communication System

Pedro A. Loureiro, Fernando P. Guiomar, Paulo P. Monteiro

Instituto de Telecomunicações, Aveiro, Portugal

pedro.a.loureiro@av.it.pt

Abstract: In this work, we present experimentally an RGB-based LD VLC system with diffused white light over 2 m of free-space distance. To evaluate its performance, the error vector magnitude per subcarrier is studied for the three colors.   © 2022 The Author(s)

1. Introduction

With the recent deployment of the 5G and the appearance of the first specifications for 6G, the required data rates are expected to be several orders of magnitude above the capacity of current wireless communication networks, mainly due to several new applications such as the internet of things (IoT) and virtual reality (VR). And as is well known, currently the sub-6GHz spectrum is completely occupied, even with efficient frequency and spatial reuse [1]. Therefore, visible light communications (VLC) is seen as a potential future solution, since the visible light spectrum has hundreds of terahertz of license-free bandwidth [2]. Thus, it can complement the mobile radio networks currently used in all locations, providing high-capacity connections. In VLC systems, the transmitter is implemented with a light-emitting diode (LED) or a laser-diode (LD). The systems with LEDs present a lower transition bit rates due to the low bandwidth of the source [3]. While with LDs the bit rates can exceed 30 Gbit/s [4].
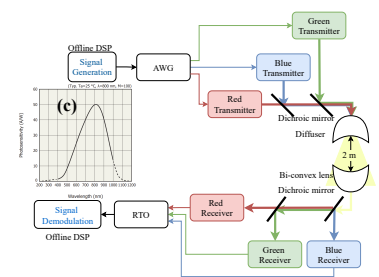
2. Experimental Demonstration

In Fig. 1 (a), we can see the architecture of the experimental setup of the VLC system. After the generation of a digital subcarrier multiplexing (SCM) signal, the waveform is generated in an arbitrary waveform generator (AWG). Three analog signals are transmitted to the LDs to modulate their light. The white light is obtained by multiplexing the red, green and blue components in the dichroic mirrors. Finally, the light is diffused to enable the illumination functionality of VLC systems. At the receiver, the three colors are demultiplexed with a bi-convex lens and two dichroic mirrors. The signals are converted back to electrical with three receiver modules. Then, in a real-time oscilloscope (RTO) the signals are digitized to be demodulated with a digital signal processing (DSP). In order to evaluate the VLC system, we analyzed the measured error vector magnitude (EVM) of 16×100 MHz signals for the red, green and blue colors. The EVM per subcarrier is depicted in Fig. 1 (b) and is obtained after transmitting a signal through the channel. Analyzing the figure, we can see that the red component outperforms the other two colors, with EVMs up to -27 dB. For the red and green colors, a flat channel up to 1 GHz is measured, which corresponds to the bandwidth of the transmitter and receiver modules. At high frequencies, a considerable penalty is verified. The blue color has a more chaotic EVM distribution due to its non-flat frequency response, having some subcarriers with an EVM close to 0 dB. These three different EVM responses are justified by the photosensitivity curve of the photodetector, as shown in Fig. 1 (c) [5]. The photosensitivity at 450 nm (blue) and 520 nm (green) are considerably lower compared to 650 nm (red).

(a) Experimental setup of the VLC system.

(b) Measured EVM per subcarrier.

Fig. 1.

3. Conclusions

We presented an RGB-based LD VLC system over 2 m free-space transmission. As shown, the red component has a better performance than the green and blue colors due to the photosensitivity curve of the photodetector.

References

1. P. H. Pathak et al., "VLC, Networking, and Sensing: A Survey ...". IEEE Com. Sur. & Tut., 2015.
2. Khan et al., "VLC: Applications, Architecture, Standardization and Research Challenges". D. Com. and Net.,2017.
3. A. M. Khalid et al., "1-gb/s transmission over a phosphorescent white led by using ...", IEEE P. Journal, 2012.
4. H. Chun et al., "A wide-area coverage 35 gb/s visible light communications link for indoor ...", Scien.c Rep., 2019.
5. Apd module c5658. accessed may 24, 2022. [Online]. Available: https://www.hamamatsu.com/eu/en/product/ optical-sensors/apd/apd-module/C5658.html.

Using multi-mode fibers to increase the tolerance to pointing errors in seamless FSO links

Manuel M. Freitas, Marco A. Fernandes, Gil M. Fernandes, Fernando P. Guiomar, and Paulo P. Monteiro

Dep. de Eletrónica, Telecomunicações e Informática, Universidade de Aveiro, e Instituto de Telecomunicações, 3810-193, Aveiro, Portugal

manuelfreitas@ua.pt

Abstract: We investigate the advantages of using a multi-mode fiber (MMF) instead of a single-mode fiber (SMF) in seamless FSO-fiber links, demonstrating that the resilience to pointing errors can be roughly doubled. © 2022 The Author(s)

1. Introduction

Free Space Optics (FSO) communications are becoming very attractive for ultra-high-capacity seamless fiber-wireless transmission in 5G and beyond communication systems, mainly due to their huge available and free-license spectrum [1]. However, one of the main challenges associated with this technology lies in the very high directivity of the optical beam, which results in pointing errors, requiring the development of highly accurate acquisition, tracking, and pointing (ATP) mechanisms for the optical beam alignment [2].

2. Free-Space Optics Link with Multi-Mode Fiber

For optimal communication, it is necessary to guarantee that the transmitter (Tx) and the receiver (Rx) are well-aligned, to avoid the pointing errors and the angle of arrival (AoA) impact. The challenge of creating a fully autonomous alignment system for the joint optimization of the Tx and the Rx depends on the power feedback received on each side. However, the starting point for the alignment process might be very challenging due to the absence of a mensurable received optical power if the initial pointing error is too high. A proficient algorithm will quickly converge to the optimum system alignment in just a few iterations when the first power threshold is found. However, the search for this value can be very slow and the success rate can be compromised. In this work, we investigate the impact of the pointing errors in an FSO link when using an MMF instead of an SMF. A 2D sweep of the beam at the Rx plane is done using two stepper motors, synchronized with a real-time power meter, see Fig. 1. For a 20 mm horizontal and vertical displacement, it can be observed that the MMF area of the optimal power values is larger than the SMF, see Fig. 2. Fig. 3. presents a cut of the power contour map that highlights the width difference between the two fibers. Considering a power threshold of -35 dBm, the tolerated beam misalignment with the SMF fiber is about 1.34 mm, which is doubled with the MMF fiber to about 2.71 mm. The MMF will help to improve the algorithm success rate and its convergence speed since its numerical aperture is larger.
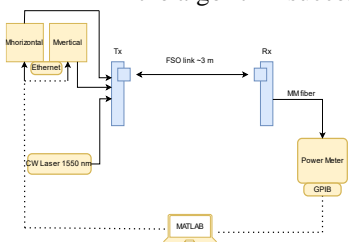
Fig. 1: Experimental setup used for automatic beam alignment.
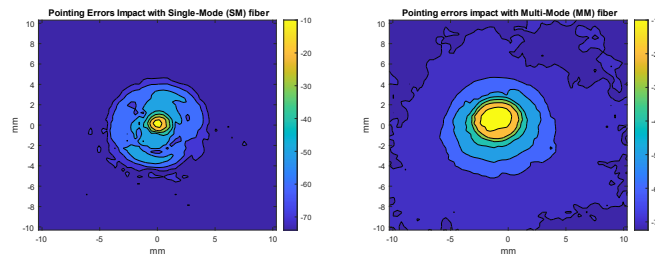
Fig. 2: SMF and MMF colormaps of power received at Rx for the different beam focus.
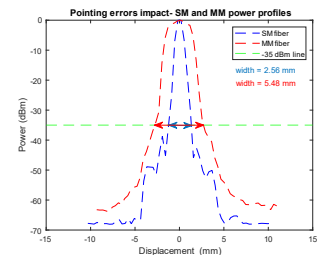
Fig. 3: SMF and MMF power penalty of beam misalignment.

3. Conclusion

This work demonstrated the advantage of using MMF to improve the robustness of FSO transmission systems to pointing errors with the objective of finding an optimal power target more easily. However, current fiber-optic communications systems are based on SMF facilitating their integration with the existing systems and subsystems.

References

[1] Marco A. Fernandes, Paulo P. Monteiro, and Fernando P. Guiomar, "Free-Space Terabit Optical Interconnects," J. Lightwave Technol. 40, 1519-1526 (2022).

[2] Marco A. Fernandes, Bruno T. Brandão, Petia Georgieva, Paulo P. Monteiro, and Fernando P. Guiomar, "Adaptive optical beam alignment and link protection switching for 5G-over-FSO," Opt. Express 29, 20136-20149 (2021).

Photonic beamforming: A SWaP-friendly solution for communication satellites

Rui Oliveira, Miguel V. Drummond, and Rogério N. Nogueira

Instituto de Telecomunicações, Aveiro, Portugal
Universidade de Aveiro, Aveiro, Portugal

ruilvo@av.it.pt (RO)

Abstract: Photonic-based beamforming has been a forefront contender in the search for lightweight and scalable solutions for communications satellite antennas. We present the past and on-going work at Instituto de Telecomunicações in this area, including first-ever achievements.   © 2022 The Author(s)

During the last 50 years, the capacity of communications satellites has increased essentially by packing more hardware in the payload. However, today's payloads are at their limits. At the same time, prioritizing capacity growth has crippled the ability to add further functionalities. Coverage flexibility is a feature that is not present in the current generation of high throughput satellites, but that is of paramount importance in today's ever-changing market needs. While mainstream electronics disciplines have not been able to resolve this deadlock, photonic technologies have emerged, aiming to finally disrupt these limitations.

While communication satellites provide the only one true ubiquitous system for internet access, they have struggled to offer competitive services compared with land-based access, in bandwidth, price and data rates. A key element in making satellite services more competitive is the use of spatial multiplexing, so that the available bandwidth can be multiplied in space, rather than divided. High density spatial multiplexing in the context of communication satellites is challenging, as the size, weight, and power consumption (SWaP) constrains are very tight. Pure electronic solutions, neither analogue nor digital, have been capable to provide this functionality at a reasonable SWaP budget that wouldn't compromise the other performance metrics of the payload [1].

Here enters photonic-based signal processing. Photonics-based signal processing has been identified as a potential solution to tackle the SWaP constraints in introducing large-scale beamforming in very-high throughput communication satellites (VHTS) [2]. The path to integrate photonics in telecommunication satellites as RF signal processors is supported by the already existent optical systems both in imaging and telecommunication satellites.

In this context, we present the past and ongoing work at Instituto de Telecomunicações in the field of photonic beamforming for satellite applications, ranging from photonic integrated circuits (PICs) to wavelength-division multiplexing (WDM)-based programmable photonic processors. We present the main achievements and first-evers that resulted from this work.

Acknowledgements

References

1. V. C. Duarte, J. G. Prata, C. F. Ribeiro, R. N. Nogueira, G. Winzer, L. Zimmermann, R. Walker, S. Clements, M. Filipowicz, M. Napierała, T. Nasiłowski, J. Crabb, M. Kechagias, L. Stampoulidis, J. Anzalchi, and M. V. Drummond, "Modular coherent photonic-aided payload receiver for communications satellites," *Nature Communications*, vol. 10, no. 1, Apr. 2019. [Online]. Available: https://www.nature.com/articles/s41467-019-10077-4
2. P. Inigo, O. Vidal, B. Roy, E. Alberty, N. Metzger, D. Galinier, J. Anzalchi, G. Huggins, and S. Stirland, "Review of terabit/s satellite, the next generation of HTS systems," in *2014 7th Advanced Satellite Multimedia Systems Conference and the 13th Signal Processing for Space Communications Workshop (ASMS/SPSC)*, Sep. 2014, pp. 318–322, iSSN: 2326-5949.

Nonlinear propagation of intense ultrashort pulses: second harmonic generation with the FDTD technique

Isabel Rodríguez Pérez [*] , **Enrique Conejero Jarque[1] and Javier Rodríguez Vázquez de Aldana[1]**

[1] *Grupo de Aplicaciones del Láser y Fotónica (ALF), University of Salamanca, Salamanca, Spain*

[*] *Corresponding author e-mail: isarodripere@gmail.com*

Abstract: We numerically study the propagation few cycles ultrashort laser pulses in linear and non-linear media with second-order nonlinear susceptibility, solving Maxwell's equations with the FDTD technique. © 2022 The Authors

Maxwell's equations describe the world of electromagnetism. Classically, the lineal response of the medium may be explained by the Lorentz model. In this model, the electrons in the material medium interacting with the external field were bound to the ions by a harmonic oscillator potential. As for the generation of the second harmonic, a quadratic term is added to the polarization. If the intensity is big enough, second harmonic generation or sum frequency generation can be generated in microscopically non-centrosymmetric materials which present second order susceptibility. There are different methods to solve these equations, our approach is based on the finite-difference time-domain (FDTD) method. This method is a flexible and powerful technique for rigorously solving Maxwell's equations. The FDTD algorithm employs second-order central differences to obtain "update equations" that express the (unknown) future fields in terms of (known) past fields [1]. The mechanism is depicted in Fig. 1 (a). The FDTD method is the simplest, both conceptually and in terms of implementation, of the full-wave techniques. It is almost completely general. We use it instead of performing asymptotic analyses or assuming paraxial propagation and nonphysical envelope functions. It permits accurate modelling of a broad variety of dispersive and nonlinear media. We numerically solve Maxwell's equations and calculate the time evolution of electromagnetic fields for different cases. We add equations to describe the dispersion [2] and nonlinearity, proportional to the square of the electric field. One example is in Fig. 1 (b) where we study the generation of the second harmonic in a medium with second-order nonlinear susceptibility.
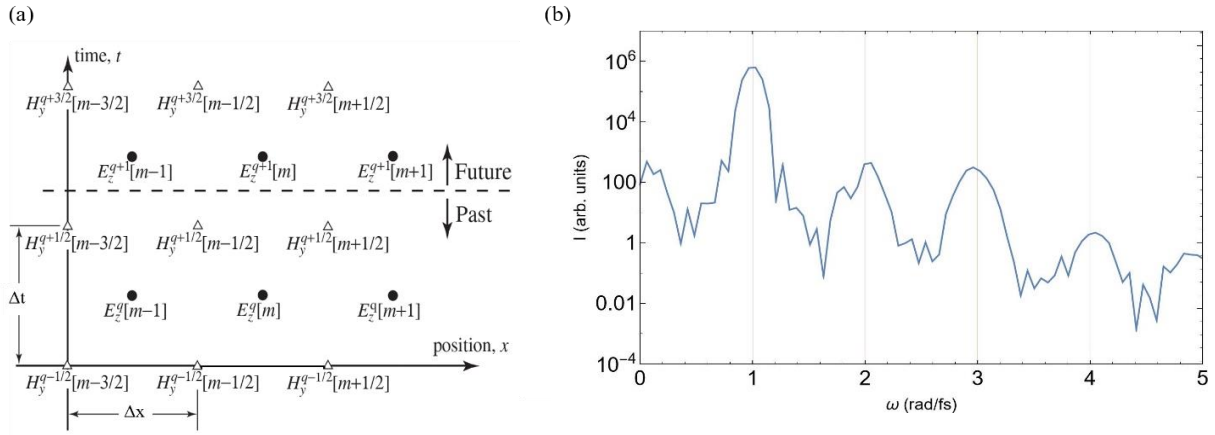
Fig. 1 (a) Scheme of the arrangement of electric- and magnetic-field nodes in space and time. (b) Pulse spectrum for the final time of our simulation. The vertical lines correspond to the fundamental frequency and second, third and fourth harmonics.

In conclusion, our theoretical simulations show how waves propagate, transmit and reflect in a variety of optical materials, with linear and nonlinear chromatic dispersion. We will present our latest results and conclusions in this research line.

References

[1] John B. Schneider "Understanding the finite-difference time-domain method", www.eecs.wsu.edu/~schneidj/ufdtd, (2010)

[2] Joseph, A. Taflove, "FDTD Maxwell's equations models for nonlinear electrodynamics and optics", IEEE Transactions on Antennas and Propagation, 45, 364 (1997)

Study of long period gratings CO_2 laser inscribing technique

A. Luís[1,*], L. Sousa[1,2], J. Vieira[1,2], M.Facão[1,3], A. Rocha[1,2]

1. Universidade de Aveiro, Aveiro, Portugal
2. Instituto de Telecomunicações, Aveiro, Portugal
3. i3N, Aveiro, Portugal
* andrefilipe.luis@ua.pt

Abstract: Here we studied the effect of the rotation and laser irradiation parameters in long period gratings (LPGs) inscription, by inscribing LPGs with different types of rotation/irradiations using a commercial CO_2 laser fiber processing system.

A long period grating (LPG) is composed by periodic changes in the refractive index of the fiber with a period of hundreds of micrometers. LPGs promote coupling between the core mode and the forward co-propagation cladding modes of the fiber at a resonant wavelength, resulting in attenuation bands in the transmission spectrum [1]. LPGs can be used not only for sensor purposes but also in devices for optical communications. Moreover, the use of LPGs to develop devices (couplers and switches) for multicore fiber (MCF) systems has been recently proposed [2]. There are different methods to inscribe LPGs, such as irradiation with UV laser, CO_2 laser or femtosecond laser, electric arc discharge or even mechanical methods [1]. In CO_2 laser irradiation technique, the silica absorbs the laser radiation heating the fiber in the incidence zone, which produces a permanent modulation of its refractive index. Thus, this inscribing technique does not require the use of photosensitive fibers or fiber pre-treatment such as hydrogen loading. In [3], it was proposed a LPG inscribing technique that uses a CO_2 laser fiber processing system (Fujikura (model LZM-100)) and the rotation of the fiber during irradiation to achieve a circularly symmetric refractive index modulation. Based on this technique, here, we study the effect of the rotation in the LPGs inscription. In this way, we inscribed LPGs in single mode fiber with four different types of irradiation/rotation: irradiation with no rotation; continuous irradiation while rotating 360º as in [3]; irradiation in two or four steps of 180º or 90º, respectively, for two different LPG periods. The values of radiation power, exposure time and fiber tension were chosen to be high enough to cause modulation of the refractive index, without deforming the fiber. These parameters were optimized for each rotation type and the best power values and exposure time used in each irradiation step are displayed in Fig 1. The transmission spectra of the inscribed LPGs for different rotations are displayed in Fig 1. For the period of 1000 μm, all the LPGs spectra present three attenuation dips around the same resonant wavelength, however the LPGs inscribed with 360º rotation and steps of 90º provided the highest attenuation dips. For the period of 1100 μm, the LPGs inscribed with rotation in steps have similar spectra and the highest attenuation dips are achieved for steps of 90º. However, the LPG inscribed with 360º rotation present a spectrum with different attenuation dips. To conclude, inscribing LPGs with 90º and 360º rotations present the best spectrum results, especially for 1000 μm, probably because of a more uniform modulation of the refractive index.
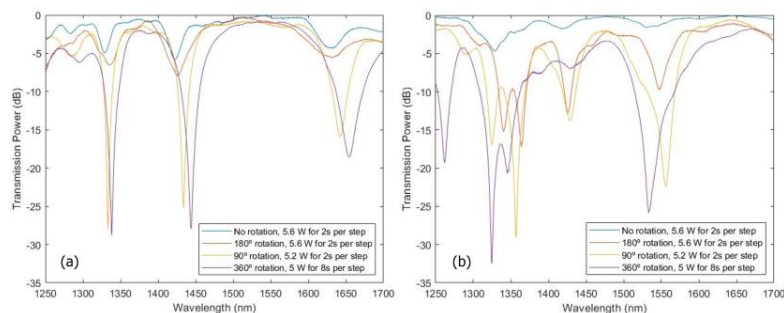
Fig 1 – LPG transmission spectra of four different samples inscribed with a period of 1000 μm (a), 1100 μm (b) for different rotations and a LPG length of 17 periods. The same initial tension was applied in all the fibers.

References

[1] S. W. James and R. P. Tatam, "Optical fibre long-period grating sensors: characteristics and application," 2003, doi:10.1088/0957-0233/14/5/201.

[2] L. M. Sousa, J. Vieira, M. Facao, G. M. Fernandes, R. Nogueira, and A. M. Rocha, "Long-Period Grating Based Coupler for Multi-Core Fiber Systems," *Journal of Lightwave Technology*, vol. 39, no. 18, pp. 5947–5953, Sep. 2021, doi: 10.1109/JLT.2021.3094298.

[3] T. Almeida, R. Oliveira, P. André, A. Rocha, M. Facão, and R. Nogueira, "Automated technique to inscribe reproducible long-period gratings using a CO_2 laser splicer," *Optics Letters*, vol. 42, no. 10, p. 1994, May 2017, doi: 10.1364/ol.42.001994.

DEVELOPMENT OF A BIDIRECTIONAL REFLECTANCE SCALE IN THE NEAR INFRARED SPECTRAL RANGE

Néstor Tejedor, Alejandro Ferrero, Joaquín Campos.

Instituto de Óptica Daza de Valdés (IO- CSIC), C/Serrano 121, 28006, Madrid, Spain.

nestor.t@csic.es

Abstract: The interest in near infrared (NIR) spectrum region has made it necessary to realize a Bidirectional Reflectance Distribution Function (BRDF) [1] standard by using the gonio-spectophotometer to develop future measurements.

1. Introduction

Due to the relevance of the near-infrared spectral range in the materials characterization, it has become necessary to realize a scale to measure the BRDF. This function describes the emerging radiance in relation to the incident irradiance on a surface when the incidence is directional.

2. Methods

The scale has been carried out on a highly reflective and diffusive ceramic sample, whose BRDF has been measured by our gonio-spectophotometer [2] in the range between 800 nm and 1700 nm. It has an illumination system consisting of a laser driven light source lamp, a monochromator, and an optical system that conducts the radiant flux to the sample. The positioning system performs the directions of incidence and collection, and consist on a robot arm together with a rotating platform, where the detection system is located. This is essentially an InGaAs photodiode, with a precision aperture. The BRDF measurement equation [3] is:

$$f_r^s(\theta_i, \phi_i; \theta_r, \phi_r; \lambda) = \left(\frac{S_r}{S_d}\right)\left(\frac{1}{\omega_r \cos\theta_r}\right);$$

the subscript d indicates the incidence signal, while the subscript r indicates the reflected signal by the sample. The solid collection angle (ωr), is measured indirectly from the sample-photodiode distance and the diameter of the precision aperture, and the cosine of the polar collection angle, r.

3. Results
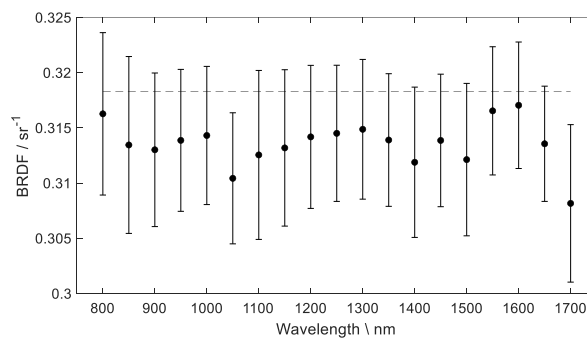
Fig. 1. BRDF (θ_i, ϕ_i, ϕ_r=0º;θ_r=45º) and uncertainty of the measured sample; discontinous line is the perfect reflecting diffuser value.

4. References

[1] F. E. Nicodemus et al., "Geometrical Considerations and Nomenclature for Reflectance. U.S. Department of Commerce", (1977).

[2] A. M. Rabal et al., Automatic Gonio-Spectrophotometer for the Absolute Measurement of the Spectral BRDF in- and out-of Plane and Retroreflexion Geometries. Metrologia, 49 (2012).

[3] A.Hope et al., "Three-dimensional appearance characterization of diffuse standard reflection materials", Metrologia 47, 295–304 (2010).

OSAC: An affordable aerosol counter for stratospheric measurements

Íñigo de Loyola Chacartegui Rojo and project ALMA

Luleå Tekniska Universitet, Space Campus, Bengt Hultqvists väg 1, 981 92 Kiruna, Sweden

igocha-1@student.ltu.se

Abstract:

This paper presents the aerosol counter developed for project ALMA on-board BEXUS33 which is based on measuring the Mie scattering of particles, especially sulphuric aerosols. The instrument provides the atmospheric vertical profile during balloon flights. © 2022 The Author(s)

1. Introduction

Project ALMA is a BEXUS student project composed by 11 members from the Lulea University of Technology based in Kiruna, northern Sweden. It is part of the REXUS/BEXUS program that give students the chance to perform experiments in either a sounding rocket or a stratospheric balloon. Therefore, we are preforming an atmospheric science experiment on board a balloon in the polar atmosphere. The main objective of the project is to find a correlation of the properties of the atmosphere in terms of the aerosol size and concentration and the ozone layer concentration and global volcanic activity in this region. To do so, we are developing the OSAC (Opens Source Aerosol Counter) to measure aerosols.

2. Methods

The OSAC working principle is based on Mie scattering theory for spherical particles: a light source (laser diode) is pointing to a sampling chamber, in which there is a flow of aerosols coming from the surroundings of the balloon. Once the aerosols cross the laser beam, they will scatter light in all directions. Part of this scattered light can be detected by placing a photo-detector at a fixed angle from the laser beam optical axis and measuring light pulses whose intensity depends on the particle properties, the wavelength of the laser, and the angle of detection.

In order to maximise the output signal from the detector for the desired size range of the particles, Mie simulations have been performed to obtain a working wavelength, detection angle and field of view for the detection. Additionally, by using the IfoCAD C++ library, an imaging system has been designed to optimise laser power distribution across the inlet pipe.

3. Results
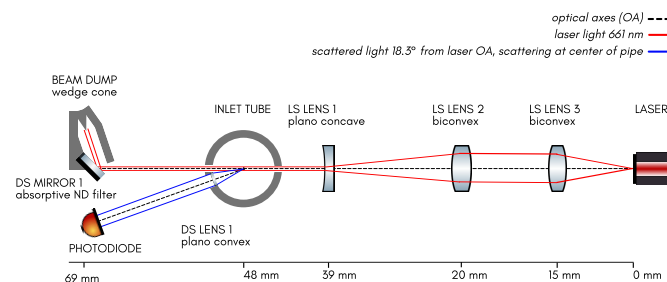
Fig. 1. Optical setup for the OSAC instrument as a result of the simulations. Composed by a Galilean telescope layout on the laser side and a single collimating lens on the detector side. The field of view for the detector is 20°.

4. Conclusion

The OSAC optical design has been defined by considering maximum intensities from Mie scattering theory. Since the design has been accepted, the practical implementation process will begin in which calibration and testing procedures will be performed.

Self-Referenced Refractive Index Sensor based on a Hollow Square Core Fiber

Diana Pereira[1,*]**, Jörg Bierlich**[2]**, Jens Kobelke**[2]**, Marta S. Ferreira**[1]

[1]*i3N & Physics Department, University of Aveiro, Campus de Santiago, 3810-193 Aveiro, Portugal*
[2]*Leibniz Institute of Photonic Technology, Albert-Einstein-Str. 9,07745 Jena, Germany*
Author e-mail address: dsap@ua.pt

Abstract: An optical fiber sensor based on a hollow square core fiber is reported to measure the refractive index of aqueous glucose solutions in a temperature varying media.
© 2022 The Author(s)

1. Introduction

The measurement of the refractive index of liquid media is of great importance for many current applications [1], since its determination allows to ascertain some compositional properties of a given solution. However, a major problem that still persists in the refractive index measurement, and has led to further investigations [2], lies on the temperature influence, in particular, the thermo-optic property of liquids. In this work, it is proposed an inline sensor based on an antiresonant microstructured hollow core fiber.

2. Methods

A hollow square core fiber (HSCF), with a squared air core with side length of $11 \, \mu m$, surrounded by silica strands with $1.7 \, \mu m$ of thickness, was used in this work. The sensor was produced by fusion splicing a $7.5 \, mm$ long of HSCF between two segments of single mode fiber. This particular configuration allows to enhance two interferometric phenomena, namely the Mach-Zehnder interferometer (MZI) and the cladding modal interferometer (CMI). Several glucose aqueous solutions, with weight percentages (wt.%) ranging from the 0 wt.% to 35 wt.%, were prepared, and put into direct contact with the entire sensing structure. To determine the sensor response to both refractive index and temperature, those solutions were later heated, and the sensor was submerged into them.

3. Results

Figure 1a presents the wavelength shift dependence with temperature of both MZI and CMI components, for all the glucose solutions that were monitored. One highlights the opposite responses of both MZI and MCI to temperature, and that, regarding the glucose concentration, the MZI response to temperature remains unaltered, while for the CMI, an increase in the sensitivity is observed. Figures 1b and 1c show the respective refractive indices of the glucose solutions, without and with temperature compensation, attained from the CMI response.
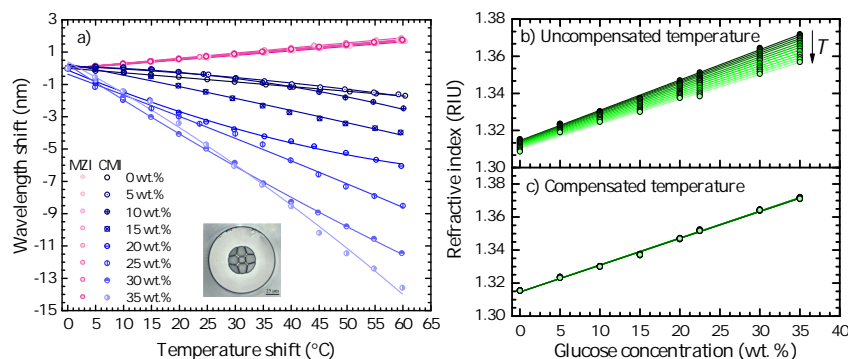
Fig. 1: (a) MZI and MCI responses to temperature. (b) Uncompensated and (c) compensated refractive index.

4. Conclusion

A simple hollow core fiber sensor was presented and revealed to be sensitive to both refractive index and temperature. Through the MZI and MCI, self-referenced refractive index measurements were achieved.

References

1. J. Li, "A review: Development of novel fiber-optic platforms for bulk and surface refractive index sensing applications," Sens. Actuators Rep. **2**, 100018 (2020).
2. V.I. Ruiz-Perez, *et al.* "Measuring the thermo-optic coefficient of liquids with athermal multimode interference devices," IEEE Sens. J., **21(3)**, 3004-3012 (2021).

In-series Fiber Bragg grating and Fabry-Pérot cavity based on adhesive based membrane on capillarity tube, for temperature compensated pressure applications

Hugo Amaral, Lúcia Bilro, Ricardo Oliveira

Instituto de Telecomunicações and Universidade de Aveiro, Campus Universitário de Santiago, 3810-193 Aveiro, Portugal
Author e-mail address: hugoamaral@.ua.pt

Abstract: In this work we propose the use of a silica fiber Bragg grating in combination with a Fabry-Pérot cavity formed by an adhesive membrane deposited on top of a silica capillary tube for hydrostatic pressure applications with temperature compensation.

1. Introduction

The opportunities of optical fiber sensors compared to electronic sensors, such as immunity to electromagnetic interference, multiplexing capabilities, compactness and their ability to be used in harsh environments, led them to be used in a variety of fields. Among the different fiber optic sensors, fiber Bragg gratings (FBGs), and Fabry-Pérot (FP) cavities, are the most used due to their easy fabrication and interrogation. Because of that, we will use both fiber technologies for hydrostatic pressure applications with temperature self-compensation.

2. Methods

We inscribed an FBG into a standard single-mode fiber (SMF) using the phase mask technology, using a 248 nm UV excimer laser. For the FP cavity fabrication, we have spliced the far end of the SMF-FBG to a 75 µm silica capillary tube, which was later cleaved with ~50 µm length. A drop of UV curable adhesive (NOA 68), was carefully placed on top of the capillary tube, allowing to form a membrane at the top. This formed three interfaces/reflectors (i.e.: SMF terminal – air (R_1); air – adhesive (R_2); and adhesive - air (R_3), which creates 3 different cavities, leading to have a spectra composed by the superposition of 3 cavities. The microscope image of the FP cavity may be seen in Fig. 1(a). The sensors were placed inside an oil pump for hydrostatic pressure characterization, which was performed in steps of 10 bar.

2. Results

In Fig. 1(b), it is shown the FP and FBG reflection spectra for each pressure step. The results show that the FP free spectral range and fringe contrast, and that the Bragg wavelength, are blue-shifted as pressure increases. The Bragg peak wavelength taken from the Bragg peak wavelength and the FP optical path length (OPL) calculated from the spectra fast Fourier transform (FFT) are shown in Fig. 1 (c).
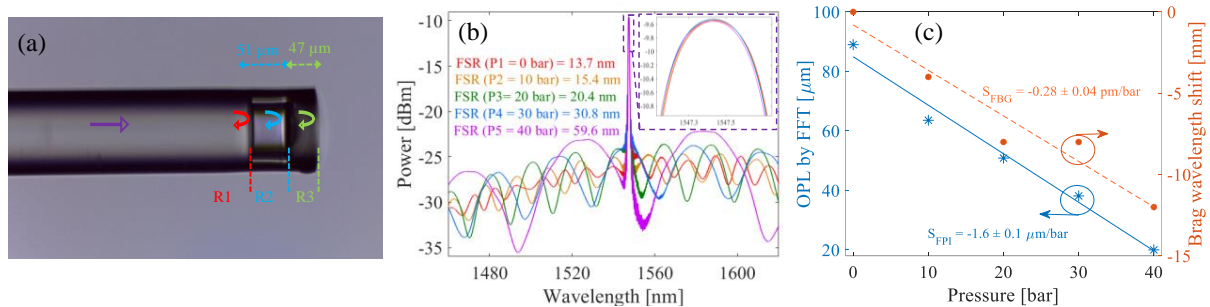
Fig. 1. (a) Microscope image of the FP cavity. (b) Spectra, and (c) OPL and Bragg-shift with pressure.

4. Conclusions

The results showed that the FBG wavelength sensitivity was ~0.3 pm/bar, which is similar to the values reported in literature. Regarding the FP cavity, it was shown a sensitivity of ~1.6 µm/bar, which demonstrates a high sensitivity performance, associated with the elasticity of the adhesive. By evaluating the sensor temperature response, it is possible to construct a 2 X 2 sensitivity matrix which will allow to simultaneously measure pressure and temperature.

Magnetic field sensing around agglomerates of magnetic nanoparticles using Nitrogen-Vacancy centers in diamond

Filipe Camarneiro[(1)], **Rajesh Tamang**[(1)], **Juanita Bocquel**[(3)], **Efres Belmonte-Reche**[(2)] **Juan Gallo**[(2)], **Manuel Bañobre-López**[(2)], **Alexander Huck**[(3)], **Jana B. Nieder**[(1)]

(1) Ultrafast Bio- and Nanophotonics, INL – International Iberian Nanotechnology Laboratory, Braga, Portugal.
(2) Nanomedicine, INL – International Iberian Nanotechnology Laboratory, Braga, Portugal.
(3) Center for Macroscopic Quantum States (bigQ), Department of Physics, Technical University of Denmark, Lyngby, Denmark
Author e-mail address: filipe.camarneiro@inl.int

Abstract: Magnetic nanoparticles can be used as heating agents in magnetic hyperthermia treatment. In this work, Nitrogen-Vacancy centers in diamond are used to measure the remaining magnetization of agglomerates of nanoparticles with nanometer-scale resolution. © 2022 The Author(s)

Introduction: Nitrogen-Vacancy (NV) centers consist of a substitutional nitrogen atom and a neighboring lattice vacancy forming well protected energy states within the bandgap. These energy states are associated with an electron spin and can be readout through the fluorescence intensity which can be influenced by temperature and magnetic fields [1]. Because of the high attainable sensitivity in the NV center fluorescence based assays, diamond biocompatibility [2], and achievable nanometer-scale spatial resolution [3], NV centers are of relevance in cell studies, diagnostics, therapeutics and material sciences. In this work, we present how NV centers in bulk diamond can be used to measure magnetic fields around magnetic nanoparticles (MNPs) with sub-micron resolution. Furthermore, we explore a second form of diamond photonics with NV centers in nanodiamonds to study magnetization of various MNPs formulations [4].

Methods: Small (< 10 nm) superparamagnetic particles were encased in a polyvinyl alcohol (PVA) film on top of a bulk diamond with a homogeneous NV center layer 5 nm away from the surface. After subjecting the sample to a strong magnetic field, Optically Detected Magnetic Resonance (ODMR) traces were taken around an agglomerate of MNPs by synchronizing the NV center fluorescence acquisition and the application of microwaves.

Results: ODMR traces taken at 500 nm steps reflect magnetic fields ranging from 0.8 to 0.03 mT within a 5 μm area around MNP agglomerates as forming during cellular uptake (Fig. 1).

Conclusions: Our results reveal that the agglomeration of small superparamagnetic particles leads to magnetic structures with persistent magnetization, due to particle-to-particle interactions, over an extended area after the application of magnetic fields. Moreover, early results using an alternative diamond platform, show the possibility of using NV centers in nanodiamonds to evaluate the magnetic state of different formulations of MNPs.
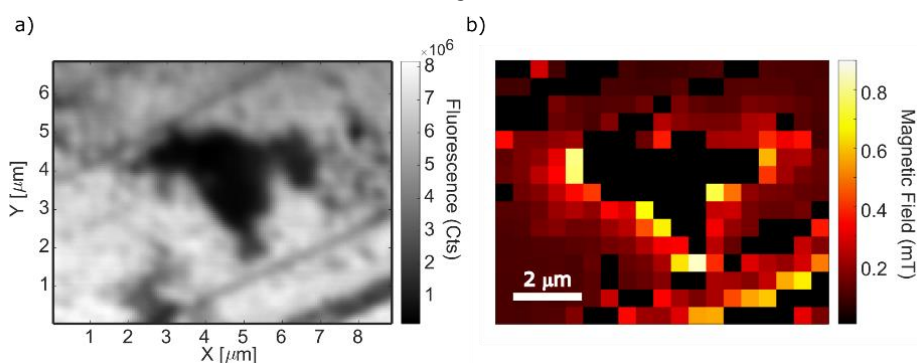
Fig. 1. Example of an agglomerate of magnetic nanoparticles; a) Fluorescence intensity image with a MNP agglomerate; b) Derived magnetic field map with magnetic field intensities ranging from 800 to 30 μT.

3. References

[1] G. Balasubramanian et al., Nature, vol. 455, no. 7213, pp. 648–651, 2008.
[2] M. Hasani et al., Small, vol. 14, no. 24, p. 1704263, 2018.
[3] F. Camarneiro et al. Particle & Particle Systems Characterization, vol. 38, no. 8, p. 2100011.
[4] F. Camarneiro, et. al. (In preparation).

Development of a Guitar Tuner Based on an Optical Fiber-FPI sensor

Francisco Silva[1], Ricardo Ferreira[1], M. Fátima Domingues[2], Paulo Antunes[1,2], Nélia Alberto[2], Tiago Paixão[1]

[1] I3N and Physics Department, University of Aveiro, Aveiro, Portugal
[2] Instituto de Telecomunicações and University of Aveiro, Aveiro, Portugal
{franciscodiogo; ricardo.a.moreira; fatima.domingues; pantunes; nelia; tiagopaixao}@ua.pt

Abstract: A guitar tuner, based on an optical fiber Fabry-Pérot interferometer (FPI), is proposed. The tuner was tested on an acoustic guitar, aiming to determine the fundamental frequencies of the notes played on the string.

1. Introduction

For an instrument to produce a pleasant sound to the ear and to capture the attention of the auditory, its tuning is essential. There are several types of tuners (tuning fork, electronic devices, software implemented on computers) [1]. However, not all have an adequate resolution to fine-tune in noisy environments, which may influence the detection of the fundamental frequencies of the instrument. Here, an optical fiber FPI-based metallic tuner is proposed to determine the fundamental frequencies of the notes played on the strings of an acoustic guitar.

2. Methods

The tuner consists of a "U" shaped metallic piece (steel), with 2 holes through which an optical fiber containing an FPI, produced from the recycling of optical fiber destroyed by the catastrophic fuse effect [2], was passed and fixed.

The tuner was placed between the bridge and the sound hole of an acoustic guitar (model APX500III, Yamaha), and the fundamental frequencies of each note (E2, A2, D3, G3, B3, E4) were determined by playing each string separately. The wavelength shift (λ) of the FPI was recorded as a function of time, as well as the fast Fourier transform (FFT) through the software ($FFT_{software}$) of the interrogation system (I-MON USB 512, Ibsen, acquisition rate of 3 kHz). Parallelly, an FFT was applied to the λ values ($FFT_{determined}$) to compare with the results given directly by the interrogation system. The deviation, N, between the fundamental frequency of the reference note (f_1) and the fundamental frequency of the note played (f_2) is given by: $N = 1200 \log_2(f_2/f_1)$ (cents) [3].

3. Results

The attained natural frequencies of the tuner were 31.74 ± 0.07 Hz ($FFT_{determined}$) and 32.04 ± 0.07 Hz ($FFT_{software}$). Fig. 1 shows an example of the wavelength variation as function of the time for the A2 note (Left), and the fundamental frequencies obtained by the analysis of the data acquired for each string are presented at the table on the right. A maximum deviation of 0.88% was achieved between the played and the reference frequencies.
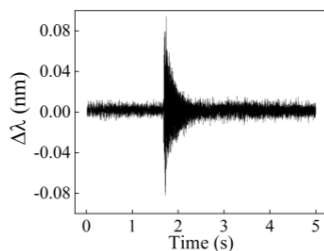
Note	Theoretical frequency (Hz) [4]	Frequency obtained (Hz)	
		$FFT_{determined}$	$FFT_{software}$
E2	82.407	85.152 ± 0.051	84.343 ± 0.007
A2	110.000	110.330 ± 0.010	110.044 ± 0.005
D3	146.832	147.639 ± 0.010	148.140 ± 0.046
G3	195.998	200.371 ± 0.031	200.145 ± 0.024
B3	246.942	250.012 ± 0.029	249.966 ± 0.026
E4	329.628	331.988 ± 0.026	332.214 ± 0.070

Fig. 1. Left) Response of the FPI-based tuner for the A2 note; Right) Fundamental frequencies obtained by the tuner.

4. Conclusion

An FPI based guitar tuner, with a theoretical resolution between 0.04-1.01 cents (units of pitch), was proposed. The attained resolution is 25 times higher than a standard commercial microphone-based tuner (1 cent), revealing to be a promising solution for guitar tuning, with the potential of being able to be used in a noisy environment.

5. References

[1] B. Bozkurt, "A system for tuning instruments using recorded music instead of theory-based frequency presets," Comput. Music J. **36**, (2012).
[2] P. Antunes et al., "Optical fiber microcavity strain sensors produced by the catastrophic fuse effect," IEEE Photonics Technol. Lett. **26**, 78-81 (2014).
[3] E. Branta et al., "Development of a triple input musical instrument tuner using Yin algorithm," Int. J. Adv. Eng, Res. Sci. **6**, 380-384, (2019).
[4] J. Rodrigues, "Bancada de ensaios para avaliação da resposta em frequência de guitarras acústicas", MSc. Thesis, 2015, http://hdl.handle.net/10400.6/5873

Hybrid Fiber Sensor Based on Capillary Tubes for Simultaneous Measurement of Pressure and Temperature

João P. Santos, Jörg Bierlich, Jens Kobelke, Marta S. Ferreira

i3N and Physics Department, University of Aveiro, Campus de Santiago, 3810-193 Aveiro, Portugal
Leibniz Institute of Photonic Technology, Albert-Einstein-Straße 9, 07745 Jena, Germany
email: jpfsantos@ua.pt

Abstract: Fiber sensors based on silica capillary tubes with access channels with Fabry-Perot interferometry and antiresonant guidance for simultaneous measurement of pressure and temperature are proposed.

1. Introduction

In this work hybrid fiber sensors based on silica capillary tubes with access channels were developed. The sensors possess an SMF-capillary-SMF/2nd capillary configuration where the interferometers Fabry-Perot (FP) and Antiresonant (AR) guidance occur simultaneously. Their response to pressure and temperature was studied.

2. Methods

The sensors were achieved through cutting and splicing the fibers. Access channels were created on the fiber sensor to function as a micro gas inlet into the capillary. One method involved performing several successive arc discharges on the capillary whilst under pressure, heating the fiber until a bubble appears. Another method included splicing the silica tube with another capillary with different inner diameter. The combination of both optical elements results in a two-access channel fiber sensor. The sensors with and without access channels were characterized to pressure in a closed chamber within the range of 0 to 0.4 MPa and to temperature with a Peltier within the range of 20 to 80 ºC.

3. Results
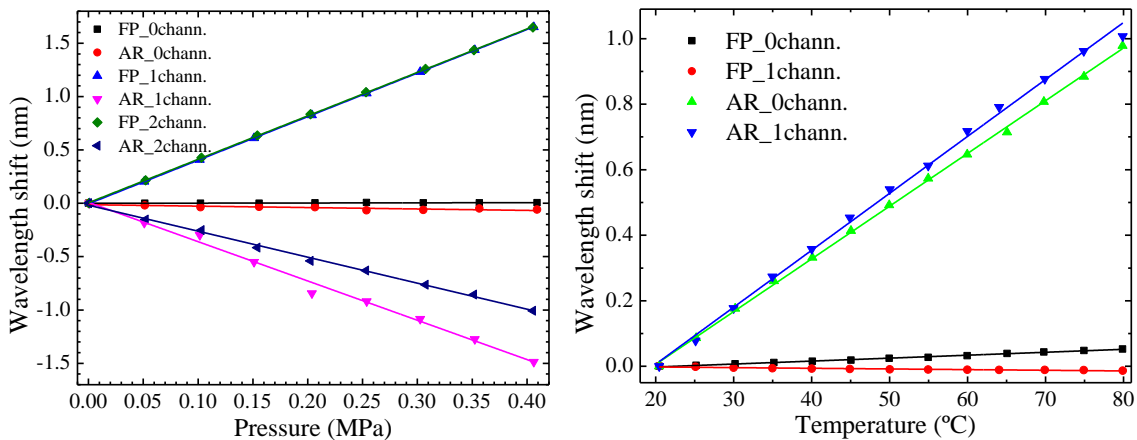
Fig. 1. Sensor response to (a) pressure and (b) temperature (length of 2 mm).

The closed sensors were insensitive to pressure. For open sensors the sensitivities were the same for FP: (4.07 ± 0.01) nm/MPa. As to the AR, the sensitivity for 1 channel was greater than for 2 channels: (3.68 ± 0.12) nm/MPa and (-2.44 ± 0.05) nm/MPa, respectively. The sensitivity to temperature was (16.09 ± 0.13) pm/°C for AR and (0.90 ± 0.02) pm/°C for FP regardless of the existence of an access channel.

4. Conclusions

In one sensing element of a few millimeters, two interferometers were observed simultaneously. The sensors were characterized to pressure and temperature. The different sensitivities of both parameters allows for a hybrid application of the sensor for simultaneous measurement of pressure and temperature.

Mode-locked erbium-doped fiber lasers

María Sánchez-Hernández[1✉], Íñigo J. Sola[1], Juan Carlos Aguado[2] and Sebastián Jarabo[3]

[1]*Grupo de Aplicaciones del Láser y Fotónica (ALF), Departamento de Física Aplicada, Universidad de Salamanca, 37008 Salamanca, Spain*
[2]*Grupo de Comunicaciones Ópticas, Universidad de Valladolid, 47011 Valladolid, Spain*
[3]*Grupo de Tecnologías Fotónicas, Universidad de Zaragoza, 50009 Zaragoza, Spain*
✉*Author e-mail address: mariash@usal.es*

Abstract: In this work, mode-locked erbium-doped fiber lasers with different kinds of active fiber have been implemented and studied. On the basis of that characterization, research dealing with an extra-cavity spectral-shifted amplification is currently in progress. © 2022 María Sánchez-Hernández, Íñigo J. Sola, Juan Carlos Aguado and Sebastián Jarabo

1. Main Text

In the last few decades, lasers with optical fiber playing the role of the active medium have been highly developed. The emission spectral range of the system, along with the compactness and feasible adaptation to different work environments, have turned out to be important contributions to a wide range of fields [1]. This interest has lately led to a broad study of the mode-locking pulsed regime [2, 3]. Thus, in this work we aim to explore and compare the implementation of a mode-locked fiber laser operating in C-band (1530-1565 nm) and L-band (1565-1625 nm) of the spectrum.

Regarding the design of the laser, it is based on an erbium-doped fiber amplifier (EDFA)- comprising the active medium (single-mode erbium-doped fiber) and the pump source (laser diode) -inside a unidirectional ring cavity from which the light is extracted by means of a 10/90 coupler. Furthermore, mode-locking is passively obtained by means of nonlinear polarization rotation, achieved introducing in the previous configuration a linear polarizer between two polarization controllers (Fig. 1(a)). The study is carried out using two different EDFAs amplifying at different spectral bands (one of them at the borderline C-L and the second one, at L-band).

Spectrum measurements have been taken from both continuous and pulsed regimes. The spectral characterization was performed with an Optical Spectrum Analyzer (OSA). Spectra of stable pulses can be seen in Fig. 1(b). Other measurements have been taken from the temporal features of the pulses down to a sensitivity of some hundreds of ps, also allowing to detect instability dynamics so we can curb them or prevent them from appearing, if needed.

Summing up, the characterization of each configuration, which can be combined with theoretical studies and simulations, provides an understanding of the system and lays the foundations for further studies. In fact, we are currently studying the effect of adding an external post-amplification stage, utilizing an EDFA with a shifted gain spectrum from the corresponding to the laser oscillator emission. Our preliminary results show substantial changes on the laser emission (e.g., spectrum), and a strong reliance on which EDFA is set as external, leading to a search for improvements to attain an optimal result. We will also present our latest results and conclusions in this research line.

2. Tables and Figures
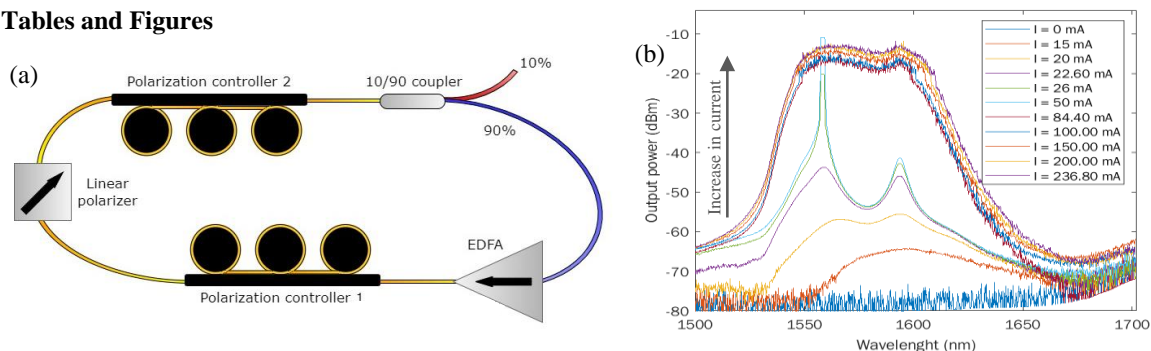
Fig. 1. (a) Pulsed regime configuration. (b) Stable pulses spectrum in the C-band limit for different pump intensities.

3. References

[1] R. Mary, D. Choudhury and A. K. Kar, "Applications of Fiber Lasers for the Development of Compact Photonic Devices," IEEE Journal of Selected Topics in Quantum Electronics 20, 72-84 (2014).
[2] Zihao Zhao, Lei Jin, Sze Yun Set, and Shinji Yamashita, "2.5 GHz harmonic mode locking from a femtosecond Yb-doped fiber laser with high fundamental repetition rate," Opt. Lett. 46, 3621-3624 (2021).
[3] N Li et al, "Mode-locked Er-doped fiber laser based on nonlinear multimode interference", Laser Phys. Lett. 17, 085105 (2020).

Optical trapping of single rare-earth ion doped upconverting nanoparticle

Fengchan Zhang[a], Marylyn Setsuko Arai[b], Andrea Simone Stucchi de Camargo[b], and Patricia Haro González[a]

[a]*Nanomaterials for Bioimaging Group (NanoBIG), Departamento de Física de Materiales, Facultad de Ciencias, Universidad Autónoma de Madrid, Madrid, 28049, Spain*

[b]*São Carlos Institute of Physics, University of São Paulo, Av. Trabalhador Saocarlense 400, São Carlos, SP, 13566-590, Brazil*

Author e-mail address: fengchan.zhang@estudiante.uam.es

Abstract: We report on the experimental observation of optical trapping of $NaYF_4$: Er^{3+}, Yb^{3+} upconverting fluorescent nanoparticles using a 980 nm single-beam laser. The laser serves both to optically trap and to excite luminescence from single nanoparticle. © 2022 The Author(s)

1. Introduction

Three-dimensional manipulation and control of single and multiple nanoparticles (tens of nanometers in size) is key for a variety of applications.[1] The lanthanide-doped upconverting nanoparticles (UCNPs) demonstrate significant advantages in bio-photonics applications.[2] In this work, we demonstrated the optical trapping and manipulation of single UCNP.

2. Methods

In the experiment, a colloidal dispersion of $NaYF_4$: $20\%\,Yb^{3+}$, $2\%\,Er^{3+}$, UCNPs in water was placed in a microfluidic chamber and excited by 980 nm diode laser. The optical force was determined by using hydrodynamic-drag method. The trapping force is calibrated against the other known force, the hydrodynamic drag force, F_{drag}, which opposes the displacement of a moving object in fluid:

$$F_{drag} = 6\pi\eta r v \qquad (1)$$

where r is the radius of the nanoparticle and η is the fluid viscosity. For each laser trapping power we measured the translating speed v required to remove the UCNPs from the trap.

3. Results

Figure 1(a) shows the transmission electron microscopy (TEM) image of the nanoparticles (90 nm in size) used in this work. Figure 1(b) shows the emission spectra of the UCNPs under different power density excitation, showing the typical Er^{3+} emission. The obtained trapping forces are shown in Fig. 1(c), showing a growing linear trend with the increased laser power. The trapping shiftiness is $4.2*10^{-4}$ pN /mW.
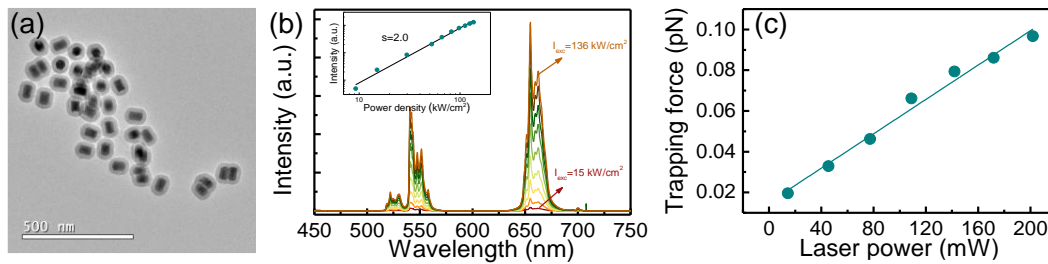
Fig. 1. (a) TEM image of the nanoparticles. (b) Upconverting emission spectra under different power density excitation. Inset shows 655 nm emission intensity versus excitation intensity. (c) Trapping force as a function of the laser power.

4. Conclusion

We have demonstrated the optical trapping of upconverting $NaYF_4$: Yb^{3+}, Er^{3+} nanoparticles by using a single 980 nm laser beam. The experimental results confirm the feasibility of single particle trapping, manipulation, and direct observation of the trapped particle thanks to the luminescence generated by the upconverting nanoparticle.

5. References

[1] P. Haro-González, B. del Rosal, L. M. Maestro, et al. *Nanoscale* 2013, 5, 12192-12199.
[2] P. Rodríguez-Sevilla, L. Labrador-Páez, P. Haro-González. *Opt. Mater.* 2018, 84, 514-523.

Plasmonic optical fiber sensors for NT-proBNP detection

Miguel Vidal[1], Ana Sofia Assunção[1], Médéric Loyez[2], Christophe Caucheteur[2], Florinda M. Costa[1], Carlos Marques[1], Sónia O. Pereira[1], Cátia Leitão[1]

[1]i3N, Department of Physics, University of Aveiro, 3810-193 Aveiro, Portugal;
[2]Electromagnetism and Telecommunication Department, University of Mons, 31 Bld Dolez, 7000 Mons, Belgium
miguelvidal@ua.pt; anasofia.matos@ua.pt; mederic.loyez@umons.ac.be; christophe.caucheteur@umons.ac.be; flor@ua.pt; carlos.marques@ua.pt; sonia.pereira@ua.pt; catia.leitao@ua.pt

Abstract: Plasmonic tilted fiber Bragg gratings and unclad tip optical fibers were tested to detect the heart failure biomarker N-terminal B-type natriuretic peptide (NT-proBNP), with the latter sensor reaching the highest sensitivity (1.61 ± 0.13 nm/log(ng/mL)).

1. Introduction

Plasmonic optical fibers have emerged as biosensors given their small size, biocompatibility, flexibility and high sensitivity [1], [2], namely tilted fiber Bragg gratings (TFBGs) [3] and unclad tip optical fibers [4]. Herein, gold-coated TFBG (Au-TFBG) and tip (Au-tip) were prepared to detect the heart failure biomarker N-terminal B-type natriuretic peptide (NT-proBNP) to assess their performance.

2. Methods

A 1 cm-long TFBG was photo-inscribed in a SMF-28 (Corning Inc.) by the phase mask technique [1], [3], while the tip sensor, 1 cm-long unclad region, was prepared from a FT200 Step-Index multimode fiber (Thorlabs) [4]. An Au layer was sputtered on both sensors [4]. Both were biofunctionalized with anti-NT-proBNP antibodies [3] via cysteamine. Then, the sensors were exposed to NT-proBNP solutions (0.01-100 ng/mL).

3. Results

The response of the TFBG and tip sensors are displayed in Fig. 1. Both sensors exhibit an increasing relationship with NT-proBNP concentration (Fig. 1a), reaching saturation for the highest values, being properly described by the Langmuir-Freundlich (LF) model. The Au-Tip achieved the largest wavelength shifts (5.42 vs 1.95 nm) and obtained a greater sensitivity in logarithmic scale (1.61 ± 0.13 vs 0.44 ± 0.04 nm/log(ng/mL)) (Fig. 1b).

(a)   **(b)**
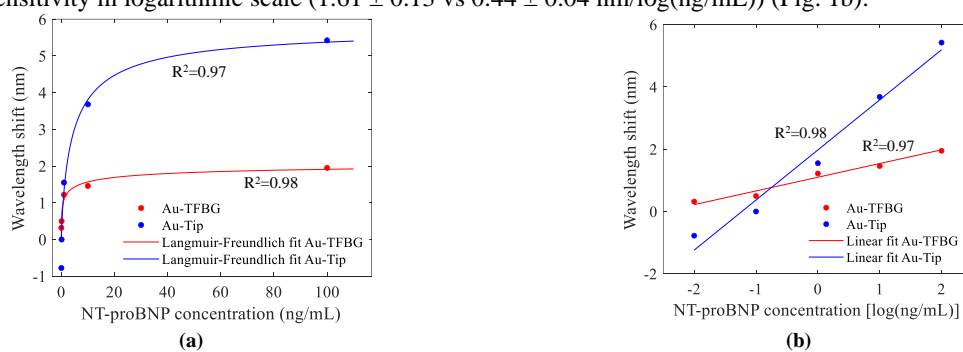
Figure 1 –Au-TFBG and Au-tip responses with (a) LF fit and (b) linear fit with the logarithm NT-proBNP concentrations.

4. Conclusions

In this work, Au-TFBG and Au-tip were tested for NT-proBNP detection, with the Au-tip achieving better sensitivity, namely 1.61 ± 0.13 nm/log(ng/mL), whilst requiring simpler spectral processing and presenting lower-cost.

5. References

[1]   M. Vidal *et al.*, "Relevance of the Spectral Analysis Method of Tilted Fiber Bragg Grating-Based Biosensors: A Case-Study for Heart Failure Monitoring," *Sensors 2022, Vol. 22, Page 2141*, vol. 22, no. 6, p. 2141, Mar. 2022, doi: 10.3390/S22062141.

[2]   M. S. Soares *et al.*, "Immunosensing Based on Optical Fiber Technology: Recent Advances," *Biosens. 2021, Vol. 11, Page 305*, vol. 11, no. 9, p. 305, Aug. 2021, doi: 10.3390/BIOS11090305.

[3]   C. Leitão *et al.*, "Cortisol In-Fiber Ultrasensitive Plasmonic Immunosensing," *IEEE Sens. J.*, vol. 21, no. 3, pp. 3028–3034, Feb. 2021, doi: 10.1109/JSEN.2020.3025456.

[4]   M. Loyez, M. Lobry, E. M. Hassan, M. C. DeRosa, C. Caucheteur, and R. Wattiez, "HER2 breast cancer biomarker detection using a sandwich optical fiber assay," *Talanta*, vol. 221, no. July 2020, 2021, doi: 10.1016/j.talanta.2020.121452.

Single-Pixel Imaging Through Phantoms by Adaptive Illumination

Erick Ipus[*,1], Armin J. M. Lenz[1], Jesús Lancis[1], Alba M. Paniagua-Diaz[2], Pablo Artal[2], Enrique Tajahuerce[1]

Author[1] GROC-UJI, Institute of New Imaging Technologies (INIT), Universitat Jaume I, 12071, Castelló, Spain
[2] Laboratorio de Óptica, Instituto de Investigación en Óptica y Nanofísica, Universidad de Murcia, E-30100, Murcia, Spain
E-mail: ipus@uji.es

Abstract: We implemented a single-pixel system by illuminating through the areas of higher transmission of the opaque medium determined previously by the characterization by means spatial frequential domain imaging (SFDI).

1. Introduction

Imaging through turbid media remains a relevant topic in biomedical imaging. When light propagates through turbid media, like biological tissue, it undergoes scattering and absorption and therefore suffers from low penetration depth. For this reason, great efforts have been made to overcome this subject in order to develop new methods for wavefront control or imaging applications [1].

Recently single-pixel imaging (SPI) has been proposed as a promising ballistic imaging technique through turbid media [2,3]. SPI is based on sampling the scene with a set of structured light patterns and the corresponding detection of the light intensity transmitted or reflected by the object with a bucket detector, without spatial resolution [4]. Typically, digital micromirror devices (DMDs) are used as spatial light modulators to codify the spatial sampling patterns.

To find the spatial locations with higher ballistic transmittance in the turbid media we use a technique based on spatial frequency domain imaging (SFDI). This technique consists in projecting sinusoidal patterns at multiple spatial frequencies with different spatial phase offsets onto the turbid media and to capture images of the diffuse reflected light. Multiple scattering and absorption will result in a decrease in the amplitude of the reflected sinewave [5]. This amplitude modulation is retrieved by a three-step demodulation method. The regions with a higher ballistic transmittance are identified as the regions with lower amplitude modulation for the high frequency sinewave and higher amplitude modulation for the low frequency sinewave.

In this work, we propose to improve the performance of a single-pixel camera in reflection geometry by projecting light patterns through the regions of the turbid media with higher transmittance of ballistic or light, avoiding areas with high absorption or scattering. This is accomplished by using a programmable light source based on an array of LEDs. The imaging system presented in this contribution combines both imaging modalities. It uses an array of LEDs as programmable light source for SFDI and a DMD as spatial light modulator for SPI. First the turbid media is characterized by means of SFDI to find the areas of higher transmittance codifying sinusoidal patterns generated in the LED array. Next, we use the light source to adapt the illumination in such a way that the light patterns generated by the DMD propagate through the best areas in the turbid media towards the object. A single pixel detector collects the light reflected by the object. The image is retrieved by applying SPI techniques, see Fig. 1.
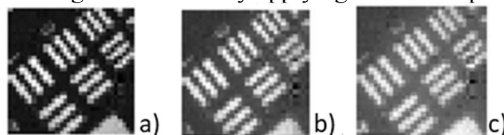
Fig 1. Images obtained, a) without turbid media, b) adapting the illumination and c) random illumination.

2. References

[1] Gigan, S., Katz, O., de Aguiar, H. B., Andresen, E. R., Aubry, A., Bertolotti, J., ... & Yılmaz, H. (2021). Roadmap on Wavefront Shaping and deep imaging in complex media. arXiv preprint arXiv:2111.14908.
[2] V. Durán, F. Soldevila, E. Irles, P. Clemente, E. Tajahuerce, P. Andrés, and J. Lancis. "Compressive imaging in scattering media." Optics Express, **23**(10):14424–14433, (2015).
[3] Rahul Dutta, Silvestre Manzanera, Adrián Gambín-Regadera, Esther Irles, Enrique Tajahuerce, Jesús Lancis, and Pablo Artal, "Single-pixel imaging of the retina through scattering media," Biomed. Opt. Express **10**, 4159-4167 (2019).
[4] Edgar, M.P., Gibson, G.M. & Padgett, M.J. "Principles and prospects for single-pixel imaging," Nature Photon **13**, 13–20 (2019).
[5] D. J. Cuccia, F. Bevilacqua, A. J. Durkin, F. R. Ayers, B. J. Tromberg, "Quantitation and mapping of tissue optical properties using modulated imaging," J. Biomed. Opt., **14**, 024012, (2009).

Shedding light on the inner workings of an optical extreme learning machine

Duarte Silva[1,2], Nuno A. Silva[1,2], Tiago D. Ferreira[1,2], Carla C. Rosa[1,2], Ariel Guerreiro[1,2]

1 Departamento de Física e Astronomia, Faculdade de Ciências, Universidade do Porto, Rua do Campo Alegre s/n, 4169-007 Porto, Portugal.

2 INESC TEC, Centre of Applied Photonics, Rua do Campo Alegre 687, 4169-007 Porto, Portugal.

duartejfs@hotmail.com, nunoazevedosilva@gmail.com, tiago.d.ferreira@inesctec.pt, ccrosa@fc.up.pt, asguerre@fc.up.pt

Abstract: Extreme learning machines are a powerful machine learning technique which can be seamlessly implemented with optical systems. Yet, it lacks fundamental understanding. In this work, a theoretical study and experimental validation is conducted in such direction.

1. Introduction

Although ultra-fast and energy-efficient optical computers are a long-standing promise of photonics, the replication of the Von Neumman paradigm faces technological limitations. Yet, the recent advent of alternative computing paradigms and in particular of Extreme Learning Machines brought new opportunities for optical computing devices, in particular for the development of specialized hardware capable of achieving significant performance gains.

2. Methods

The underlying concept of an extreme learning machine (ELM) is a random and nonlinear projection of the information $\{x_i\}_{i=1}^N$ into a high-dimensional output space, $h_i(x) = G(a_i, b_i, x)$, where the activation function G is a nonlinear piecewise continuous function. For a specific target function $f(x): R^d \to R^m$, we can construct a prediction in the output space as $f_{ELM}(x) = \sum_{i=1}^L \beta_i h_i(x)$, where the vector β is trained through ridge regression:

$$\min_{\beta \in R^{L \times m}} \left|\left| H\beta - T \right|\right|_2^2 + \lambda \left|\left| \beta \right|\right|_2^2 \quad , \qquad (1)$$

where $H_{ij} = h_j(x_i)$, $T_{ij} = (y_i)_j$ is the target data given a training set $\{x_i, y_i\}_{i=1}^N$, and $|| \cdot ||_2$ denotes the frobenius norm. By training only a linear transformation at the output layer, this paradigm becomes particularly attractive for physical implementation and hardware specialization and thus suitable for an all-optical implementation.

In Fig.1 we present an illustration of the concept and experimental setup. In short, a digital micromirror device works as our optical encoder, before the light being coupled to a multi-mode fiber where the information is mixed. At the output, a speckle pattern is measured on a CCD camera, constituting the output space.

3. Results and discussion

Using the transmission matrix formalism, we developed a theoretical framework that demonstrates that simple linear dynamics followed by intensity measurements yield an effective activation function of polynomial and/or sinusoidal nature. This theoretical framework was validated experimentally, in particular by exploring the correlation between the rank of the outputs, H, and its generalization capability. In addition, we have studied the effect of strong non-linearities on the machine, through standard regression and classification benchmarks, allowing to conclude that the system constitutes an optical extreme learning machine. The findings enclosed in this work pave the way for a greater understanding of such devices, allowing for a better design and task selection.
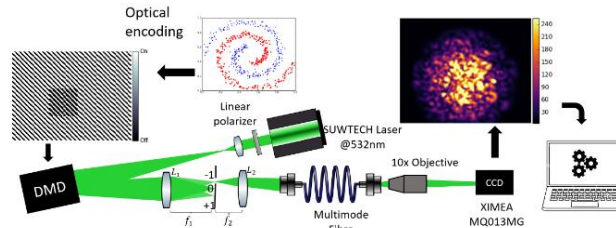
Fig. 1. Illustration of the optical set-up and methods for an optical extreme learning machine

4. References

[1] A. Saade et al. "Random projections through multiple optical scattering: Approximating Kernels at the speed of light". 2016 IEEE International Conference on Acoustics, Speech and Signal Processing (ICASSP).

[2] Guang-Bin Huang, Qin-Yu Zhu, and Chee-Kheong Siew. "Extreme learning machine: a new learning scheme of feedforward neural networks". 2004 IEEE International Joint Conference on Neural Networks.

Accommodative schematic eye models: A review

María Mechó García, , José M. González-Méijome.

Clinical and Experimental Optometry Research Lab (CEORLab), Center of Physics, School of Sciences, University of Minho, Braga, Portugal
mmechogarcia@fisica.uminho.pt

Abstract: This review aimed to summarize the schematic accommodative models that have been described by various authors over the past years. Focusing on the similarities and differences used by each of them. © 2022 María Mechó García, José M. González-Méijome

Introduction: A schematic eye model is a simplified version of the human eye based on a mathematical or physical model. These classical models consist in fixed parameters based on a population average. Some of these models are able to describe the accommodative ability of the human eye, and these may be of great interest because they are able to explain the functionality of the human eye, represent its basic optical properties and are useful for research purposes.

Methods: A review of the scientific literature on accommodative schematic models was carried out. Different databases were used for this purpose: PubMed, Scopus, Embase and Web of Science. The date of the search was not restricted. Different combinations of keywords ("accommodative model" OR "schematic model") AND ("accommodative" OR "Accommodation") were used to perform the search.

Results: The classification described by Esteve-Taboada et al. (2018) was followed. In it, two different groups are differentiated, the paraxial schematic models (assume constant refractive indices, the surfaces are assumed to be spherical and are centred on a common axis) and the finite models which try to reproduce the optical characteristics of real eyes (having aspherical surfaces, variation of the gradient index of the crystalline lens and their optical surfaces are not centred on a common optical axis). The schematic eye models have fixed properties that represent the optical properties of a number of human eyes, although of all those proposed the most flexible is the reduced Indiana model, which allows for axial and lateral variation of the pupil, allowing for variation of various reference axes of the eye.

Conclusions: There is currently no perfect schematic accommodative model, although each may be ideal for different applications. Limitations of most of these models is that the physiological and morphological parameters are based on averages values so they fail to capture the inter-individuals variability as well as the changes with aging or after surgical procedures and other factors.

[1] Esteve-Taboada JJ, Montés-Micó R, Ferrer-Blasco T. Schematic eye models to mimic the behavior of the accommodating human eye. J Cataract Refract Surg. **44(5),** 627–41 (2018).

[2] Thibos LN, Hong X, Bradley A, Cheng X. Statistical variation of aberration structure and image quality in a normal population of healthy eyes. J Opt Soc Am A Opt Image Sci Vis. **19(12)**, 2329-48 (2002).

[3] Thibos LN, Bradley A, Hong X. A statistical model of the aberration structure of normal, well-corrected eyes. Ophthalmic Physiol Opt. **22(5),** 427–33 (2002).

[4] Navarro R. Adaptive model of the aging emmetropic eye and its changes with accommodation. J Vis.**14(13)**, 21–21 (2014).

[5] Popiolek-Masajada A, Kasprzak HT. A new schematic eye model incorporating accommodation. Optom Vis Sci Off Publ Am Acad Optom. **76(10)**, 720–7, (1999).

[6] Navarro R, Santamaria J, Bescós J. Accommodation-dependent model of the human eye with asphcrics. JOSA A. **2(8)**, 1273–80 (1985).

Clinical validation of simulated multifocal IOLs. SimVis Gekko[TM] simulations vs literature data from implanted patients

Amal Zaytouny[1], Irene Sisó-Fuertes[2], Xoana Barcala[1, 2], Lucie Sawides[2], Carlos Dorronsoro[2], Susana Marcos[1, 3]

1. *Instituto de Óptica, CSIC. Calle Serrano 121, 28006 Madrid, Spain*
2. *2EyesVision, Plaza de la Encina, 10, 28760 Tres Cantos, Madrid, Spain;*
3. *Center for Visual Science, The Institute of Optics, Flaum Eye Institute, University of Rochester, New York, USA*

amal.z@csic.es

Abstract: TF-VA curves were measured in presbyopic patients through SimVis Gekko[TM] simulating M-IOLs. Results were compared with literature data from patients implanted with the same IOLs, demonstrating that the simulator can capture the real vision through intraocular corrections.

1. **Introduction**

   A large variety of intraocular lens (IOL) designs is commercially available in the market, and selecting the best option is key for a positive surgical outcome. SimVis Gekko[TM], a see-through simultaneous vision simulator, allows patients to see the real world through different corrections prior to surgery. Through focus visual acuity (TF-VA) curves are commonly measured in the clinic to assess presbyopic corrections in pseudophakic patients. Several reports compare post-operative TF-VA curves of different lens designs to analyze the visual performance of different multifocal IOLs (M-IOLS).

2. **Methods**

   Three commercial M-IOL designs were programmed in SimVis Gekko[TM] from on bench optical quality publicaly available data: AcrySof IQ Vivity (Alcon), AT Lisa and AT Lara (ZEISS). Binocular TF-VA curves (from -4.0 to +1.50 D, in 0.50 steps) were measured through SimVis Gekko[TM] simulations in a total of 7 healthy presbyope participants (age: 54.5 ± 5 years; spherical error: 1.03 ± 1.22 D; astigmatism ≤ 0.75 D) and results from the simulations were then compared to the postoperative TF-VA from implanted patients (Vivity (n=107), AT Lisa (n=81) and AT Lara (n=30) as reported in the scientific literature.

3. **Results**

   Overall, there was a good match between SimVis Gekko[TM]-simulated and implanted TF-VA curves. VA results obtained at far distance with the Vivity/ ATLisa/ ATLara M-IOLs through the SimVis simulations at far were -0.08 ± 0.03/-0.08 ± 0.03/-0.07 ± 0.02, and -0.02/0.00/0.00 in implanted patients, respectively. At intermediate distance (defocus range from -2.00 D to -0.50 D), differences in logMAR VA between real M-IOLs and simulations were -0.06/-0.08/-0.13, and at near distance (defocus range from -4.00 D to -2.00 D), were -0.2/-0.02/0.2 for the three M-IOLs. In the range of -3.0 D to 1.0 D defocus, the shape similarity metric (cross correlation) between simulations and real lenses was 0.94, 0.93 and 0.77 for the Vivity, AT Lisa and AT Lara M-IOLs respectively.

4. **Conclusions**

   The match of TF-VA performance between presbyopic subjects through SimVis Gekko[TM]-simulated M-IOLs and patients implanted with the corresponding commercial lenses suggests that corrections can be programmed in the simulator using publicaly available data and reliably simulate them to reproduce the real vision through the Vivity, AT Lisa, and AT Lara M-IOLs. SimVis was also able to capture the differences across the designs assessed.

In vitro and computational characterization of daily multifocal soft contact lenses for visual simulations using SimVis Gekko

Eduardo Esteban-Ibañez[1,2], Diego Montagud-Martínez[3,4], Lucie Sawides[2], David P. Piñero[5], Walter D. Furlan [3], Enrique Gambra[2].

1. Institute of Optics, Spanish National Research Council (IO-CSIC), Madrid, Spain. 2. 2EyesVision SL, Madrid, Spain. 3.Departamento de Óptica, Universitat de València, Burjassot, Spain. 4. Centro de Tecnologías Físicas, Universitat Politécnica de València, Valencia, Spain 5. Departamento de Óptica, Universidad de Alicante, Alicante, Spain.

eesteban@2eyesvision.com

Abstract: Four families of daily soft MCLs were characterized by in vitro measurements and computational methods, obtaining sufficient data to simulate them correctly with SimVis Gekko in the fitting guides' process.

1.Introduction

The SimVis Technology (SimVis Gekko® by 2EyesVision SL, Madrid, Spain) has demonstrated its ability to accurately simulate multifocal lens designs for both intraocular lenses[1,2] and contact lenses (CLs) [3].

For an easy fitting of multifocal contact lenses (MCLs), manufacturers provide specific fitting guides dedicated to their MCLs, with different steps in function of patient's parameters. The replication of fitting guides with SimVis Gekko could provide an improvement in this process, allowing to test quickly different designs in only one session. The purpose of this work is to characterize four daily multifocal soft contact lenses families for the posterior replication of their fitting guides using SimVis Gekko simulations.

2.Methods

The power profiles of four families of daily soft MCLs from different manufacturers: MyDay® Multifocal (Coopervision), Biotrue® ONEday for Presbyopia (Bausch+Lomb), 1-Day Acuvue® Moist Multifocal (Johnson & Johnson) and Dailies Total1® Multifocal (Alcon), were measured using NIMO TR-1504 (Lambda-X, Belgium) across a 7 mm diameter optical zone and immersed in saline solution. All families were measured three times for all additions (Low, Medium and High Addition) and five nominal powers: +4.00, +2.00, 0.00, -2.00 and -4.00 D (except for BioTrue ONE® day and 1-Day Acuvue® Moist which were only measured for -2.00, 0.00 and +2.00D). The power profiles obtained with the NIMO were used to compute the MCLs phase maps for three different diameters of 3, 4 and 5 mm, and the Through-Focus Visual Strehl (TFVS) obtained using the process already described in Vinas et al.[3]

3.Results

All described MCLs were successfully measured with NIMO and the TFVS was computed for three different pupil sizes. Fig. 1 shows some examples of TFVS considering pupil size, manufacturer, lens refraction and addition.
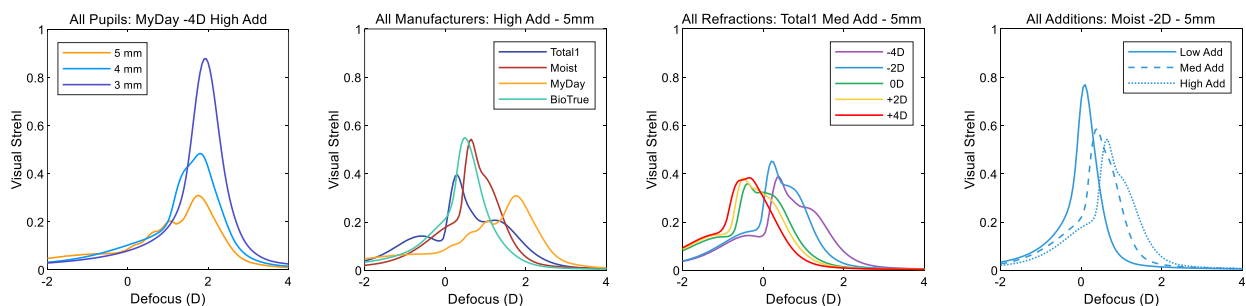

Fig. 1. Examples of TFVS (from left to right) across pupil sizes, manufacturers, lens refractions and additions.

4.Conclusions

The characterization of different MCLs families, refractions and additions with NIMO and the computation of their TFVS for different pupil sizes allow to obtain the correct and necessary MCLs simulations to perform the fitting guide*s'* process using SimVis Gekko.

5.References

[1] Dorronsoro C, Radhakrishnan A, Alonso-Sanz JR, Pascual D, Velasco-Ocana M, Perez-Merino P et al. Portable simultaneous vision device to simulate multifocal corrections. Optica. 2016;*3*(8):918-924.

[2] Vinas M, Benedi-Garcia C, Aissati S, Pascual D, Akondi V, Dorronsoro C, et al. Visual simulators replicate vision with multifocal lenses. Sci Rep. 2019;9(1):1–11.

[3] Vinas M, Aissati S, Gonzalez-Ramos AM, Romero M, Sawides L, Akondi V et al. Optical and visual quality with physical and visually simulated presbyopic multifocal contact lenses. Transl Vis Sci Technol. 2020;9(10):1-16.

Multispectral Fluorescence Lifetime Imaging with Single-Pixel Cameras and Data Fusion

A. J. M. Lenz[1,*]**, F. Soldevila**[2]**, A. Ghezzi**[3,4]**, A. Farina**[4]**, C. D'Andrea**[3,5]**, and E. Tajahuerce**[1]

[1]*GROC-UJI, Institute of New Imaging Technologies (INIT), Universitat Jaume I, Castelló, Spain.*
[2]*Laboratoire Kastler Brossel, École Normale Supérieure – Paris Sciences et Lettres (PSL) Research University,*
Sorbonne Université, Centre National de la Recherche Scientifique (CNRS), Collège de France, Paris, France.
[3]*Politecnico di Milano, Dipartimento di Fisica, Milano, Italy.*
[4]*Consiglio Nazionale delle Ricerche, Istituto di Fotonica e Nanotecnologie, Milano, Italy.*
[5]*Istituto Italiano di Tecnologia, Center for Nano Science and Technology, Milano, Italy.*

[*]maxemili@uji.es

Abstract: We present a technique for multispectral fluorescence lifetime imaging with high spatial resolution by combining both single-pixel and data fusion imaging techniques. The resultant 4D hypercube can be used to identify fluorophore species. © 2022 The Author(s)

1. Introduction

In this contribution, we present a technique that combines single-pixel imaging (SPI) and data fusion techniques to capture high spatial resolution, multispectral, and time-resolved fluorescence images [1, 2]. The system relies on the combined use of three different sensors: two SPI cameras capturing multispectral and time-resolved information, and a conventional 2D array detector capturing high spatial resolution images (see Fig. 1(a)). Data fusion techniques are introduced to combine the individual 2D/3D projections acquired in parallel by each sensor in the final 4D hypercube. The fusion procedure is done by solving a regularization problem which can be efficiently solved via gradient descent.
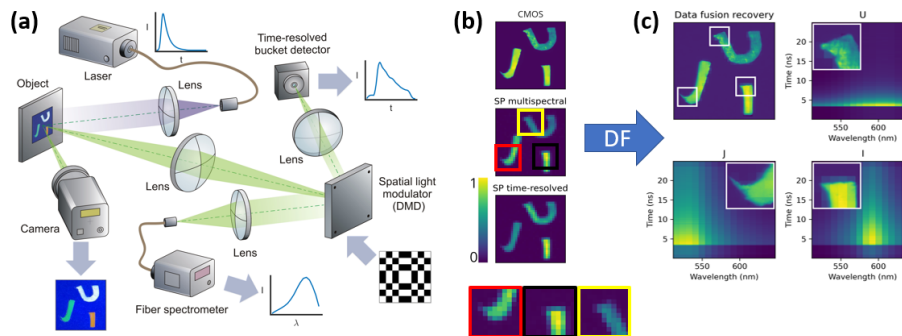

Fig. 1. (a) Optical implementation of the system. (b) Spatial projections of the three measured datasets. (c) Results from the data fusion algorithm.

2. Results

The sample is a 4D object with three different fluorophores distributed in different letters. We acquired a 512×512 pixel image with the CMOS camera. The multispectral SPI camera obtained a 32×32×16 datacube (32×32 pixels with 16 spectral channels). The time-resolved SPI camera is based on a Hybrid-PMT connected to a time-correlated single- photon counting (TCSPC) board, and provided a 32×32×256 datacube (32×32 pixels with 256 time intervals). Fig. 1 (b) shows the spatial projection of the measured datasets obtained by the three sensors. Results from the DF algorithm are shown in Fig. 1(c) [3].

References

1. M. P. Edgar, G. M. Gibson, and M. J. Padgett, "Principles and prospects for single-pixel imaging," Nat. Photonics (2018).
2. B. Khaleghi, A. Khamis, F. O. Karray, and S. N. Razavi, "Multisensor data fusion: A review of the state-of-the-art," Inf. Fusion **14**, 28 (2013).
3. F. Soldevila, A. J. M. Lenz, A. Ghezzi, A. Farina, C. D'Andrea, and E. Tajahuerce, "Giga-voxel multidimensional fluorescence imaging combining single-pixel detection and data fusion," Opt. Lett. **46**, 4312-4315 (2021).

SILK FIBROIN FILMS FOR CORNEAL HEALING: TOWARDS OPTIMAL PHOTOBONDING PARAMETERS

Rocio Gutierrez-Contreras[1], Fernando Zvietcovich[1], Andres de la Hoz[1], Irene E. Kochevar[2], Judith S. Birkenfeld[1], Susana Marcos[1]

[1]Instituto de Óptica Daza de Valdés, IO-CSIC, C/ Serrano 121, 28006 Madrid, Spain
[2]Wellman Center for Photomedicine, Massachusetts General Hospital, Boston, Massachusetts, United States
Author e-mail address: rocio.gutierrez@csic.es

Abstract: Sutured amniotic membrane is as a standard-of-care treatment of injured corneas. We proposed Silk fibroin based membranes as an alternative corneal bandage fixed to the cornea through a light-initiated sutureless procedure.

1. Main Text

Introduction

Amniotic membrane (AM), generally attached to the cornea by sutures, is a standard treatment for corneal abrasions [1]. However, it can provoke immune response, is generally opaque, and it tends to be scarce and expensive. Silk fibroin (SF) has low immunogenicity, it is abundant and affordable compared to AM. We have developed SF membranes to be attached to the cornea through a light-initiated sutureless method [2]. Two different types of SF membranes were tested.

Methods

SF was extracted from silk cocoons with a standard process [3]. Two different membranes were casted and crosslinked, with polyethylene glycol (SF-PEG) or ethanol (SF-EtOH). The Young's modulus was calculated by stretching 3x10 mm strips in a uniaxial stretcher. SF strips (3x15 mm) were soaked in Rose Bengal (RB) (10^{-4} - 0.01 %), placed on top of rabbit corneal strips and irradiated with green light (0.019 - 0.075 W/cm^2) [4]; (0.25 - 6.6 min). Bonding forces were measured using a uniaxial stretcher. Control membranes were irradiated without RB staining. Rabbit eyes were also used to test the membrane bonding under various intraocular pressure (IOP) conditions. One cm-diameter SF-PEG membranes were peripherally photobonded (0.01% RB; 0.075 W/cm^2 for 0.5 – 3.3 min) on 1.5 mm perforated corneas. IOP was increased from 5 mmHg until initial detachment of the membrane is observed (IOP^D), using an optical coherence tomography (OCT) imaging system.

Results

Photobonded SF-EtOH strips experienced increased bonding forces with RB irradiation dosage (Fig. 1). Lower RB concentration and longer irradiation time induced a stronger bonding, likely as a result of RB shielding of the bonding interphase, an effect that decreases with lower concentration. For the same conditions, SF-PEG strips deformed before detachment. These strips needed as low as 0.019 W/cm^2 for 0.25 minutes and 10^{-4} % RB to be strongly bonded (>0.1N) to the cornea. The IOP^D increased with irradiation time, from 25 to 85 mmHg for 0.5 to 3.3 minutes irradiation. Uniaxial stretching experiments showed that the Young's Modulus of SF-EtOH's was twice that of SF-PEG (10MPa).

Conclusion

Bonding forces can be modulated by adjusting RB concentration and irradiation time. Membranes peripherally photobonded resist IOPs higher than the physiological range (10 – 20 mmHg). These results establish the required parameters to carry out *in vivo* photobonding of SF membranes in rabbit eyes.
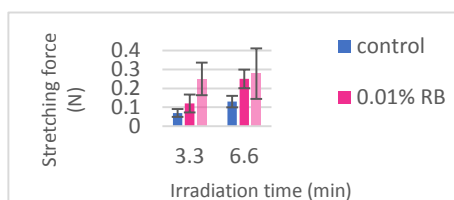
2. Tables and Figures

Figure 1. Bonding forces after irradiating SF-EtOH + corneal strips at 0.075 W/cm^2 for different times and RB concentration.

3. References

[1] Dua HS *et al*. The amniotic membrane in ophthalmology. *Surv. Ophthalmol*. 2004 Jan-Feb;49(1):51-77.
[2] De la Hoz A *et al*. Photobonded silk-fibroin films for corneal dressing. *IOVS*. 2019;60(9):3218.
[3] Rockwood D *et al*. Materials fabrication from *Bombyx mori* silk fibroin. *Nat Protoc* **6,** 1612–1631 (2011).
[4] Zhu H *et al*. Corneal Crosslinking With Rose Bengal and Green Light: Efficacy and Safety Evaluation. *Cornea*. 2016 Sep;35(9):1234-41.

Perceiving the original colors of images of natural scenes changed by the atmosphere over the distance of observation

Andreia E. Gomes, João M.M. Linhares and Sérgio M.C. Nascimento

Physics Centre of Minho and Porto Universities (CF-UM-UP), Gualtar Campus, University of Minho, 4710-057 Braga (Portugal)

Author e-mail address: andreia.gomes.ni@gmail.com

Abstract: The visual ability to retrieve the original chromatic content of complex images simulating the effect of atmospheric optics at several viewing distances was estimated. Results revealed that original chromatic content can be retrieved with good accuracy.

1. Main Text

1.1. Contextualization and Purpose

Light undergoes scattering and absorption when it passes through the atmosphere, decreasing perceived contrast and chromatic diversity with distance, thereby changing the way objects and scenes are perceived as the viewing distance increases. However, it is unclear which visual chromatic information can be recovered from images modified by the presence of atmospheric effects and how much those effects can be empirically reduced by the visual system. The purpose of this study was to measure the influence of the atmospheric effects on viewing conditions and to verify if they could be empirically reduced by a human observer.

1.2. Experimental methods

A psychophysical experience was performed to estimate if a normal color vision observer could retrieve the original colorimetric content of images simulated for an arbitrary viewing distance considering the correspondent atmospheric effects. 11 hyperspectral images of complex natural scenes were used to simulate their colors for distances from -200 to 2000 m using a precise physical model of the effects of atmosphere [1], as shown in Figure 1. Negative values represented an increment of the original saturation both in color and luminance. The simulated images were presented in a CRT monitor calibrated in color and luminance in steps of 50 m viewing distance. 54 observers with normal color vision and no visual abnormities had to select an image correspondent to a desired simulated distance by using a remote control. In experiment 1 the observer should choose the image that looked more natural and in experiment 2 the one that looked unnatural, starting from the original image. In other words, finding the first image with detected changes from the original one. A Gaussian fit was performed to the frequency of the distances selected by the observers, and the position of the maximum of assumed as the distance selected.

1.3. Results and Conclusions

Data across scenes and observers showed that the viewing distance selected with higher frequency as most natural was +17±16 m considering the entire data from -200 to +2000 m, and – 2±13 m considering only the range -200 to +200 m. These distances are very close to zero suggesting that despite the changes induced by the atmosphere to the chromatic diversity of natural scenes with the increment of the viewing distance, these observers are sensitive to changes in the naturalness of colors due to atmospheric effects and can retrieve the original chromatic information of changed images with good accuracy.

2. Tables and Figures

Figure 1: Rendering of one of the images simulated for different observational distances. Numbers in each scene indicates the correspondent distance in meters. Negative values represent images closer to the original acquisition distance, representing colors with higher saturation.

3. References

[1] Romero, J., Luzón-González, R., Nieves, J. L., & Hernández-Andrés, J. (2011). Color changes in objects in natural scenes as a function of observation distance and weather conditions. *Applied Optics*, *50*(28), F112-20.

3D non-linear micro-imaging of femtosecond laser induced damage tracks in crystals

María J. Martínez-Morillo✉, Javier R. Vázquez de Aldana, and Ignacio López-Quintás
Grupo de Investigación en Aplicaciones del Láser y Fotónica (ALF), University of Salamanca, Salamanca, Spain
✉*Author e-mail address: mjmm53@usal.es*

Abstract: Second-harmonic microscopy allows obtaining high-resolution three-dimensional images without the need for confocal set-ups nor fluorescence labels. We have applied this microscopy technique to the 3D analysis of femtosecond laser damage tracks in non-linear crystals. © 2022 The Author(s)

Non-linear microscopy [1,2] is an imaging technique that allows high-resolution 3D reconstructions of samples without the need for confocal set-ups and without the use of fluorescence labels. It is a scanning technique in which a short-pulsed laser is focused on the sample. The emerging signal of different wavelength generated as a consequence of an optical non-linear process, either parametric (second or third harmonic generation, SHG/THG) or via non-linear fluorescence, is detected for each position, thus obtaining an emission map. The reconstruction of the signal obtained from different planes allows three-dimensional imaging of biological samples [3] and other non-linear structures [4].

On the other hand, femtosecond lasers have been established as very versatile tools for 3D micro-structuring of transparent dielectrics [5]. High-power pulses can be focused inside those samples so that intensities capable of inducing non-linear absorption and ionisation processes are reached in the focal zone, leading to the formation of a free electron plasma. Once the interaction with the laser is over and the material relaxes, as a consequence of these processes, a damage track is left on the material, which results in a localised (microns) and controllable modification of the refractive index. This capability of ultrashort laser pulses is very useful in applications such as waveguide inscription [6].

In this work, the second harmonic generation process is used to study the micro-modifications previously induced in a non-linear crystal with a femtosecond laser. The micro-modifications are induced in a BBO crystal by focusing 800 nm, 60 fs pulses delivered at 5 kHz of repetition rate through a 40X microscope objective. Irradiation was performed 15 μm below the surface at increasing pulse energies from 0.04 and 0.2 μJ. The crystal is scanned at 100 μm/s to form damage tracks. The sample is then analysed in a home-made second harmonic microscope, measuring the forward and backward signals at 400 nm, and analysing the effect of the incident laser polarization.

In conclusion, our studies show that the SH microscopy is a suitable technique for 3D imaging of structures. The different emission levels are interpreted in terms of the presence of defects created in the damage zone, as well as possible densifications in areas close to the damage tracks.
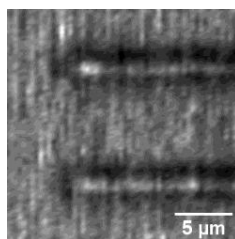

Fig. 1. SHG-Forward signal image of two damage tracks inscribed in a BBO crystal with 0.2 μJ/pulse and located 15 μm below the surface.

References

[1] C. Sheppard and R. Kompfner, "Resonant scanning optical microscope", Applied Optics **17**, 2879 (1978).
[2] I. Freund and M. Deutsch, "Second-harmonic microscopy of biological tissue", Optics Letters **11**, 94 (1986).
[3] X. Chen, O. Nadiarynkh, S. Plotnikov, and P. Campagnola "Second harmonic generation microscopy for quantitative analysis of collagen fibrillar structure", Nature protocols **7**, 654 (2012).
[4] C. Hu, J. Field, V. Kelkar, B. Chiang, K. Wernsing, K. Toussaint, R. Bartels and G. Popescu, "Harmonic optical tomography of nonlinear structures". Nature Photonics **14,** 564 (2020).
[5] R. Gattas and E. Mazur, "Femtosecond laser micromachining in transparent materials", Nature Photonics **2**, 219 (2008).
[6] F. Chen and J.R. Vázquez de Aldana, "Optical waveguides in crystalline dielectric materials produced by femtosecond-laser micromachining", Laser and Photonics Reviews **8**, 251 (2014).

Microscopy with optical sectioning by single pixel detection

Luis Ordóñez*, Erick Ipus, Jesús Lancis, Enrique Tajahuerce
GROC-UJI. Institute of New Imaging Technologies (INIT), Universitat Jaume I, 12071, Castelló, Spain
*e-mail: lordonez@uji.es

Abstract: We present a single-pixel microscope with optical sectioning by combining two structured illumination methods: structured illumination microscopy and single-pixel imaging. Experimental results are shown for the application on bright-field and fluorescence microscopy. © 2022 The Author(s)

1. Introduction

The impact of microscopy has undergone an enormous advance in science. This could not be possible without new technologies that can increase the image resolution, allow us to measure many optical parameters such as the fluorescence emission, optical phase, wavelength, or polarization state, permit high-speed capture rates, and improve the penetration capability in scattering media [1]. In this work we design a microscope with optical sectioning properties by combining two structured illumination techniques: structured illumination microscopy (SIM) and single-pixel imaging (SPI). As a first application we introduce optical sectioning capability on single-pixel fluorescence microscopy.

SIM techniques increase the image resolution and provides sectioning capability in conventional microscopy methods [2]. By projecting a small number of high frequency periodic fringe patterns with different phase onto the sample and combining the obtained images with the proper phase-shifting algorithm, it is possible to exclude the out of focus areas from the final image.

SPI techniques scan the scene with a set of structured light patterns while the transmitted, reflected, or fluorescence light is detected with a bucket detector [3]. They are advantageous for multidimensional imaging as well as in situations where the amount of light is scarce, or a high temporal resolution is required [3]. In our optical configuration we use a DMD to project the light patterns onto the sample, which codify Walsh-Hadamard functions, and a photomultiplier tube (PMT) to detect the fluorescence light emitted by the sample.

Combining SIM and SPI makes optical sectioning possible in imaging with a bucket detector. The key idea is to employ a grating located before the photodetector. This configuration is designed starting from the conventional SIM configuration and exploiting the principle of Helmholtz reciprocity.

2. Results and conclusion

Preliminary results of the fluorescent SPI and SIM techniques are presented (Fig. 1.) The sample is a set of cotton fibres with green fluorescent ink. Figures 1(a) and (b) show images of the sample focused on different depths, with an axial separation of 10 μm, obtained with a conventional single-pixel microscopy. The two images show cotton fibres located at different distances that appear strongly defocused. Figures 1(c) and (d) show images of the same planes of the sample but obtained with the new single-pixel microscopy technique. Now only the focused cotton fibres in each axial plane are clearly visible. All images have a size of 128x128 pixels.

In summary, we present the principles and implementation of a SPI fluorescence microscope with optical sectioning based on a SIM technique. By combining the high-speed binary modulation of the DMD, a high frequency grating, and the high photosensitivity of the PMT, we are able to image fluorescence samples using structured illumination. Our experimental results show an optical sectioning capability similar to that obtained with conventional SIM techniques with a digital camera.

Fig. 1. **(a)** and **(b)** are images of cotton fibres obtained with conventional single-pixel microscopy for two different focusing planes located at $z = 0$ and $10\mu m$, respectively. **(c)** and **(d)** are images of the same sample planes obtained with optical sectioning.

3. References

[1] J. Mertz; *Introduction to Optical Microscopy* (Cambridge University Press, 2019).
[2] D. Dan et al., "DMD-based-LED-illumination super-resolution and optical sectioning microscopy," Sci. Rep. **3**, 1116 (2013).
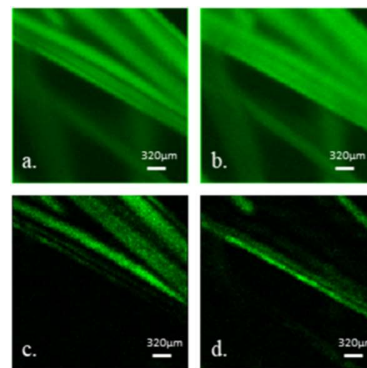[3] M.P. Edgar et al., "Principles and prospects for single-pixel imaging," Nat. Photon. **13**, 13-20 (2019).

Color Variation in Translucent Materials

Pablo Santafé-Gabarda*, Alejandro Ferrero, Joaquín Campos

Institute of Optics "Daza de Valdés", Spanish National Research Council. C/ Serrano 121, 28006 Madrid, Spain.
*pablo.santafe@csic.es

Abstract: The variation of the Bidirectional Reflectance Distribution Function (BRDF) regarding the illumination area has been related with the illumination wavelength to study the consequent color variation of translucent samples. © 2022 The Authors.

1. Introduction

The BRDF was defined by Nicodemus et al. [1] as it follows:

$$f_r(\mathbf{r}_i; \mathbf{r}_r) = \left. \frac{dL_r(\mathbf{r}_i; \mathbf{r}_r)}{dE_i(\mathbf{r}_i)} \right|_{A_i \text{ large enough}}, \tag{1}$$

where f_r denotes the BRDF, dL_r is the differential element of the reflected radiance, dE_i is the differential element of the irradiance on the surface, $\mathbf{r}_i$ and $\mathbf{r}_r$ are the irradiation and collection directions, respectively, and A_i is the irradiation area on the surface, which has to be much larger than the mean free path of the light inside the material.

2. Methods

The BRDF of three translucent samples (A, B, C, in order from most opaque to most transparent) has been measured with five different irradiation areas and the same measurement geometry, represented in Fig. 1 (a). For each irradiation area, six equally-spaced irradiation wavelengths have been used to obtain a spectrum of the reflected light. These measures were carried out with the gonio-spectrophotometer of the Institute of Optics of the CSIC [2].
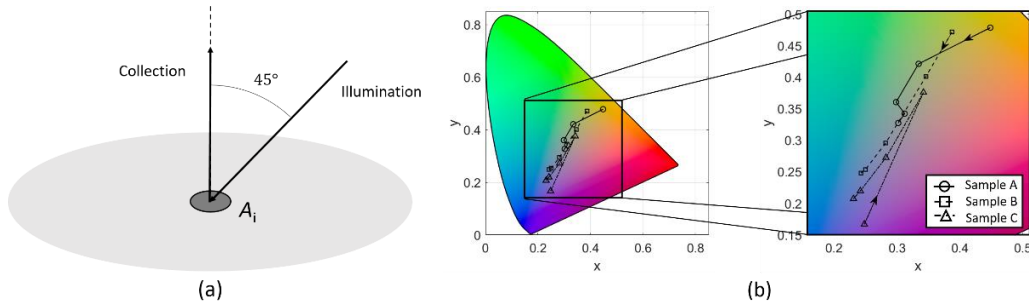

Fig. 1. (a) Scheme of the measurement geometry. (b) Measured color of each sample with each irradiation area, calculated with the D65 illuminant and the CIE 1931 standard observer. The arrows indicate the increasing way of the irradiation area.

3. Results

The color coordinates in the CIE 1931 color space, with the D65 illuminant, of each sample with each irradiation area have been calculated from the BRDF. They are represented in Fig. 1 (b), where it is shown that the measured color of the surface of the translucent samples varies with the irradiation area.

3. Conclusions

It has been proved that the measured color of the surface of a translucent material may vary when different irradiation areas are used. Thus, it is necessary to stablish some procedures to measure the color of translucent samples.

4. References

[1] F. E. Nicodemus, J. C. Richmond, J. J. Hsia, I. W. Ginsberg, and T. Limperis, *Geometrical Considerations and Nomenclature for Reflectance* (U.S. Department of Commerce, 1977).

[2] A. M. Rabal, A. Ferrero, J. Campos, J. L. Fontecha, A. Pons, A. Rubiño, and A. Corróns, "Automatic goniospectrophotometer for the absolute measurement of the spectral BRDF at in-and out-of-plane and retroreflection geometries", Metrologia 49(3), 213–223 (2012).

Precise calibration of a LiDAR based on stereoscopic imaging and a projected dot pattern

João Alegria*, Paulo P. Monteiro, Miguel V. Drummond

Department of Electronics, Telecommunications and Informatics, University of Aveiro,3810-193 Portugal
Instituto de Telecomunicações, University of Aveiro, Campus Universitário de Santiago, 3810-193 Portugal
author: joaoalegria31@ua.pt

Abstract: In this paper, it is presented a short description of an inexpensive LiDAR model. The main idea revolves around on how precise can it be. The paper goes through the working steps into achieving a precise stereoscopic LiDAR. © 2022 The Author(s)

1. Introduction

Although self-driving cars have been around for a few years, the practical side is still blurry. LiDAR is the most capable sensor in providing a detailed view of the surroundings but the price is still prohibitive for manufactures. Using a stereoscopic vision setup (fig. 1) composed of a pair of stereo and a laser it is possible to estimate distances employing trigonometry.
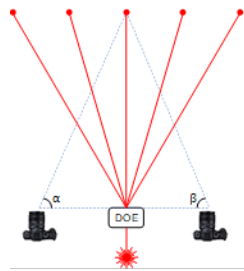

Fig. 1. Stereoscopic LiDAR setup

For this inexpensive LiDAR to be useful, it must be very precise and thus very well calibrated. In this contribution, the objectives and work plan will be presented in order to achieve that.

2. Work plan

Starting from the question "How good is OpenCV's calibration?", it is assessed whether OpenCV [1] can achieve near ideal calibration with ideal parameters. The method for calibration used will be Zhang's [2] since it is proven to be the overall best and easiest to use. The next step is to develop a realistic calibration setup in python, considering real camera parameters and pixelization. The third step is to translate the previous step to reality and see how the two compare. Finally is would be interesting to draw conclusions from the results obtain with the current state of the art LiDARs.
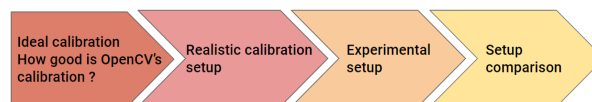

Fig. 2. Work plan

References

1. OpenCV. Opencv: Camera calibration and 3d reconstruction. "https://docs.opencv.org/3.4/d9/d0c/group__calib3d.html, 2022. [Online; accessed 26-April-2022].
2. Zhengyou Zhang. A flexible new technique for camera calibration. 13, 2008.

All-digital ADC for an automotive LiDAR receiver

Laura F. Cabete[*], Daniel Bastos, Miguel V. Drummond, Paulo P. Monteiro

Department of Electronics, Telecommunications and Informatics, University of Aveiro, 3810-193, Aveiro, Portugal
Instituto de Telecomunicações, University of Aveiro, Campus Universitário de Santiago, 3810-193, Aveiro Portugal
[*]Corresponding author: lfcabete@ua.pt

Abstract: The feasibility of an all-digital Analog-to-Digital Converter (ADC) for sampling Light Detection and Ranging (LiDAR) signals is addressed. Implementation in a single Field Programmable Gate Array (FPGA) is proposed, obliterating cost and power consumption issues. © 2022 The Author(s)

To fulfill its main purpose of autonomously travel in an ecosystem composed of several other stationary and moving objects and beings, self-driving cars must be able to reliably observe its surroundings. Several different vision sensors complement each other, leading to this ability of measure and reconstruct a faithful representation of its surroundings at every instant, with LiDAR being a key one, as it is able to provide a detailed point cloud of the 3D view around it. Each point of the point cloud is obtained based on the time of flight (ToF) of a pulse fired to the scene, reflected by it and captured again by the sensor. This is why the range, precision and accuracy of a LiDAR sensor mainly depend on how each of these received pulses is captured, sampled and processed.

Considering that, to construct a reliable point cloud, a LiDAR receives tens or even hundreds of signals and each of them needs to be sampled, it is crucial to design ADCs in such a way that having tens or hundreds of them working simultaneously in a LiDAR system does not become prohibitive in terms of cost and power consumption. This is the main purpose of this project: to demonstrate that an all-digital ADC able to correctly sample LiDAR signals can be implemented in a single FPGA, without any expensive or power consuming external components added. Following previous work on all-digital ADCs development for other purposes [1,2], the scheme of the proposed all-digital ADC is represented in Fig. 1a. and the signals expected to be obtained in each stage in Fig. 1b.
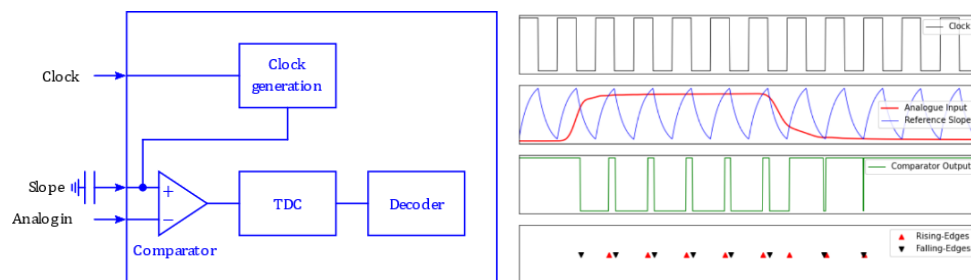

Fig.1. (a) Scheme of the proposed all-digital ADC. (b) Signals at each point of the scheme.

A realistic numerical model of the proposed all-digital ADC is being developed, with the goal of applying it to a dataset comprising realistic LiDAR waveforms produced in a lab environment. Such an approach shall enable comparing the proposed all-digital ADC with any other ADC, namely an ideal ADC. Preliminary results show that sampled waveforms are identical for the all-digital ADC and for an ideal ADC, preserving all the characteristics defined as central for the chosen estimation method to work properly.

The final goal is clear: to implement a simple, low power and cost-effective ADC, while preserving the estimation accuracy, precision and reliability required for automotive LiDAR.

References

[1] Homulle, H., Regazzoni, F., & Charbon, E. (2015). 200 MS/s ADC implemented in a FPGA employing TDCs. In FPGA 2015 - 2015 ACM/SIGDA International Symposium on Field-Programmable Gate Arrays (pp. 228–235).

[2] Leuenberger, L., Amiet, D., Wei, T., & Zbinden, P. (2021). An FPGA-based 7-ENOB 600 msample/s adc without any external components. In FPGA 2021 - 2021 ACM/SIGDA International Symposium on Field-Programmable Gate Arrays (pp. 240–250).